JOURNAL OF GEOPHYSICAL RESEARCH, VOL. 108, NO. E12, 8086, doi:10.1029/2002JE002035, 2003

Rock size-frequency distributions on Mars and implications for Mars Exploration Rover landing safety and operations

M. P. Golombek,[1] A. F. C. Haldemann,[1] N. K. Forsberg-Taylor,[2] E. N. DiMaggio,[3]
R. D. Schroeder,[4] B. M. Jakosky,[5] M. T. Mellon,[5] and J. R. Matijevic[1]

Received 19 December 2002; revised 8 June 2003; accepted 11 July 2003; published 21 October 2003.

[1] The cumulative fractional area covered by rocks versus diameter measured at the Pathfinder site was predicted by a rock distribution model that follows simple exponential functions that approach the total measured rock abundance (19%), with a steep decrease in rocks with increasing diameter. The distribution of rocks >1.5 m diameter visible in rare boulder fields also follows this steep decrease with increasing diameter. The effective thermal inertia of rock populations calculated from a simple empirical model of the effective inertia of rocks versus diameter shows that most natural rock populations have cumulative effective thermal inertias of 1700–2100 J m^{-2} $s^{-0.5}$ K^{-1} and are consistent with the model rock distributions applied to total rock abundance estimates. The Mars Exploration Rover (MER) airbags have been successfully tested against extreme rock distributions with a higher percentage of potentially hazardous triangular buried rocks than observed at the Pathfinder and Viking landing sites. The probability of the lander impacting a >1 m diameter rock in the first 2 bounces is <3% and <5% for the Meridiani and Gusev landing sites, respectively, and is <0.14% and <0.03% for rocks >1.5 m and >2 m diameter, respectively. Finally, the model rock size-frequency distributions indicate that rocks >0.1 m and >0.3 m in diameter, large enough to place contact sensor instruments against and abrade, respectively, should be plentiful within a single sol's drive at the Meridiani and Gusev landing sites. *INDEX TERMS:* 6225 Planetology: Solar System Objects: Mars; 5470 Planetology: Solid Surface Planets: Surface materials and properties; 5464 Planetology: Solid Surface Planets: Remote sensing; 5460 Planetology: Solid Surface Planets: Physical properties of materials; *KEYWORDS:* Mars Exploration Rover landing sites, Mars Pathfinder landing site, thermal inertia, rocks, Gusev, Meridiani

Citation: Golombek, M. P., A. F. C. Haldemann, N. K. Forsberg-Taylor, E. N. DiMaggio, R. D. Schroeder, B. M. Jakosky, M. T. Mellon, and J. R. Matijevic, Rock size-frequency distributions on Mars and implications for Mars Exploration Rover landing safety and operations, *J. Geophys. Res.*, *108*(E12), 8086, doi:10.1029/2002JE002035, 2003.

1. Introduction

[2] Understanding the size-frequency distribution of rocks on Mars is important for a number of reasons. First, rocks on the surface of a planet and a landing site in particular result from the geological processes that have formed that surface, so that characterizing the population of rocks may lead to a better understanding of the geomorphologic and geologic history of the site [e.g., *Garvin et al.*, 1981]. Rocks are also a prime science target for roving vehicles designed to determine the mineralogy and geochemistry of a location on Mars. Second, rocks on the surface of a planet represent an obvious and real hazard to landing spacecraft and a potential impediment to roving. The better the rock size-frequency distribution of Mars can be understood, the better the potential hazards to landers can be described and quantified [e.g., *Golombek and Rapp*, 1997]. Prior to the Mars Pathfinder landing, *Golombek and Rapp* [1997] found that the size-frequency distribution of rocks at the Viking landing sites and a number of rocky locations on Earth all could be fit with simple exponential curves, which are compatible with fracture and fragmentation theory (see discussion and references by *Golombek and Rapp* [1997]). Fits of data at the Viking landing sites yield a model that describes the size-frequency distribution of rocks at any location where the total rock abundance can be estimated from remote infrared thermal measurements [*Christensen*, 1986a]. This work, coupled with extensive testing of the Pathfinder airbag landing system [*Golombek et al.*, 1997a], allowed an estimate of what total rock abundances (percentage of the surface covered by rocks) derived from thermal differencing techniques [*Christensen*,

---

[1] Jet Propulsion Laboratory, California Institute of Technology, Pasadena, California, USA.

[2] Department of Environmental Sciences, University of Virginia, Charlottesville, Virginia, USA.

[3] Department of Geological Sciences, University of Michigan, Ann Arbor, Michigan, USA.

[4] Department of Geology, California State University, Bakersfield, California, USA.

[5] Laboratory for Atmospheric and Space Physics, University of Colorado, Boulder, Colorado, USA.

0148-0227/03/2002JE002035

1986a] could be considered safe for landing. In addition, this general function was used to correctly predict the overall size-frequency distribution of rocks as well as the number of large, potentially hazardous boulders at the Mars Pathfinder landing site [*Golombek and Rapp*, 1997; *Golombek et al.*, 1997a, 1999b].

[3] In this paper, we use a number of approaches to further test and constrain the rock size-frequency distribution of rocks on Mars and the model derived by *Golombek and Rapp* [1997] and use this information to calculate the probability of impacting potentially hazardous rocks at the Mars Exploration Rover (MER) landing sites. To start, we will present the first complete description of the rock fields observable from the Mars Pathfinder lander, which will include counts of rocks within the near field (generally within 10 m of the lander) and large rocks in the far field (beyond 10 m). Second, we will use boulders visible in high-resolution Mars Orbiter Camera (MOC) images to characterize the shape of the rock size-frequency distribution at large rock diameters (>3 m). Third, we will use observed rock size-frequency distributions to derive the effective thermal inertia of natural rock populations with special reference to potentially hazardous rocks. Fourth, we will compare the distributions of rocks on Mars with those used in MER airbag drop tests. Fifth, we will characterize the shape and burial of the rocks, which is important to airbag performance, at the Viking 1 (VL1), Viking 2 (VL2) and Mars Pathfinder (MPF) landing sites and the rocks used in the airbag drop tests. Finally, we will use the size-frequency distributions and assessment of rock shape and burial to estimate the probability of impacting potentially hazardous rocks and the accessibility of rocks by MER at the prospective landing sites.

2. Rock Distributions at the Mars Pathfinder Landing Site

2.1. Introduction

[4] The size-frequency distribution of rocks at the Mars Pathfinder landing site (Figure 1a) was determined for rocks in the near field (out to about 10 m from the lander) and in the far field (beyond 10 m). The distinction between near and far field is primarily determined by the techniques used to assemble the data. Two independent counts were made in each case. The first near- and far-field counts were carried out during Mars Pathfinder operations and discussed briefly by *Golombek et al.* [1997b, 1999b]. Here we present details of more complete and careful near- and far-field rock counts describing methods and the resulting size-frequency distributions. The newer work supercedes the earlier results, which are incorrect.

2.2. Near-Field Measurements

2.2.1. ShowstereoMap Database

[5] The first near-field rock data were limiting in that only two rock population parameters, apparent width and height, were evaluated in addition to rock position. In order to carry out more detailed studies of the rock population in the vicinity of the Pathfinder lander, we built a new rock database with more spatial information for each rock, including nine local-level frame coordinates to evaluate rock position and shape, as well as descriptive parameters like shape, which in the sedimentological literature includes form or sphericity, angularity or roundness, and surface texture [*Barrett*, 1980], and burial and color. A number of interns (“rock-counters”) used the JPL-developed “showstereo” image analysis software to determine the spatial parameters for each rock. We thus call these data the “ShowstereoMap near-field rock database.” The showstereo software performs user interactive stereo matching of individual image pairs. We chose image pairs from the entire post mast deployment IMP data set that provided the best available resolution (lowest compression) for that part of the rock field. Generally these are red (670 nm) Superpan images, although some blue (440 nm) Superpan images, and even some Monsterpan images were used [*Golombek et al.*, 1999a]. Five shape (technically form or sphericity) categories (discoidal, subdiscoidal, spherical, subprismoidal, and prismoidal) and the six angularity categories (very angular, angular, subangular, subrounded, rounded, and well-rounded) were measured for each rock following accepted sedimentological grain shape studies [e.g., *Krumbein*, 1941; *Barrett*, 1980; *Dobkins and Folk*, 1970; *Sneed and Folk*, 1958; *Pye*, 1994]. Burial of each rock was a qualitative assessment [e.g., *Baron et al.*, 1998] ranging from perched to partially buried to deeply buried (these data are summarized later in this paper). Texture was characterized according to the criteria of *Parker et al.* [1998] for bumpy, pitted, knobby, smooth, and lineated textures [*Drake*, 1970] based on examination of the rock appearance in images. Color was determined only for the larger rocks using separate software to generate average DN values for the rock faces from full-color IMP image sets. All data were hand-entered via a web-interface into a mySQL database [*Widenius and Axmark*, 2002].

[6] The final ShowstereoMap database includes 4454 rocks. For the vast majority of these rocks (4307) the showstereo software generated the spatial information, and the data set is thus consistent for statistical mapping purposes. Corrections were made for about 75 larger rocks that fall across image boundaries. Also, position measurements using a vicar software routine [*Duxbury and Jensen*, 1994] called “mpfview” were made for some dark near-field images (147 rocks in 17 images). Mpfview, unlike showstereo, allows for image processing in addition to stereo analysis, so it was used for rock color determinations, however it was not used extensively because its interface was less conducive to database entry. Of all the measurements, 24 rocks measured in a single image pair with mpfview could not be reconciled with the image pointing and were removed from the mapping and statistical analysis that follows. A map of the 4430 measured rocks is shown in Figure 1b. We calculate the rock field statistics in a rough annulus from 2.5 m to about 8.5 m radius shown by the dashed line on Figure 1b with an area of 199.7 m^2. In addition, portions of the annulus are obscured by foreground rocks. To determine the obscured area, we examined the digital terrain map of *Kirk et al.* [1999] to find areas where they did not map stereo coordinate points. A contouring of these stereo voids at 0.25 m resolution gives an obscured area in the annulus of 13.25 m^2, producing a normative area for rock statistics of 186.4 m^2. There is uncertainty in this approach to determining the obscured area, although doubling the obscured area estimate only

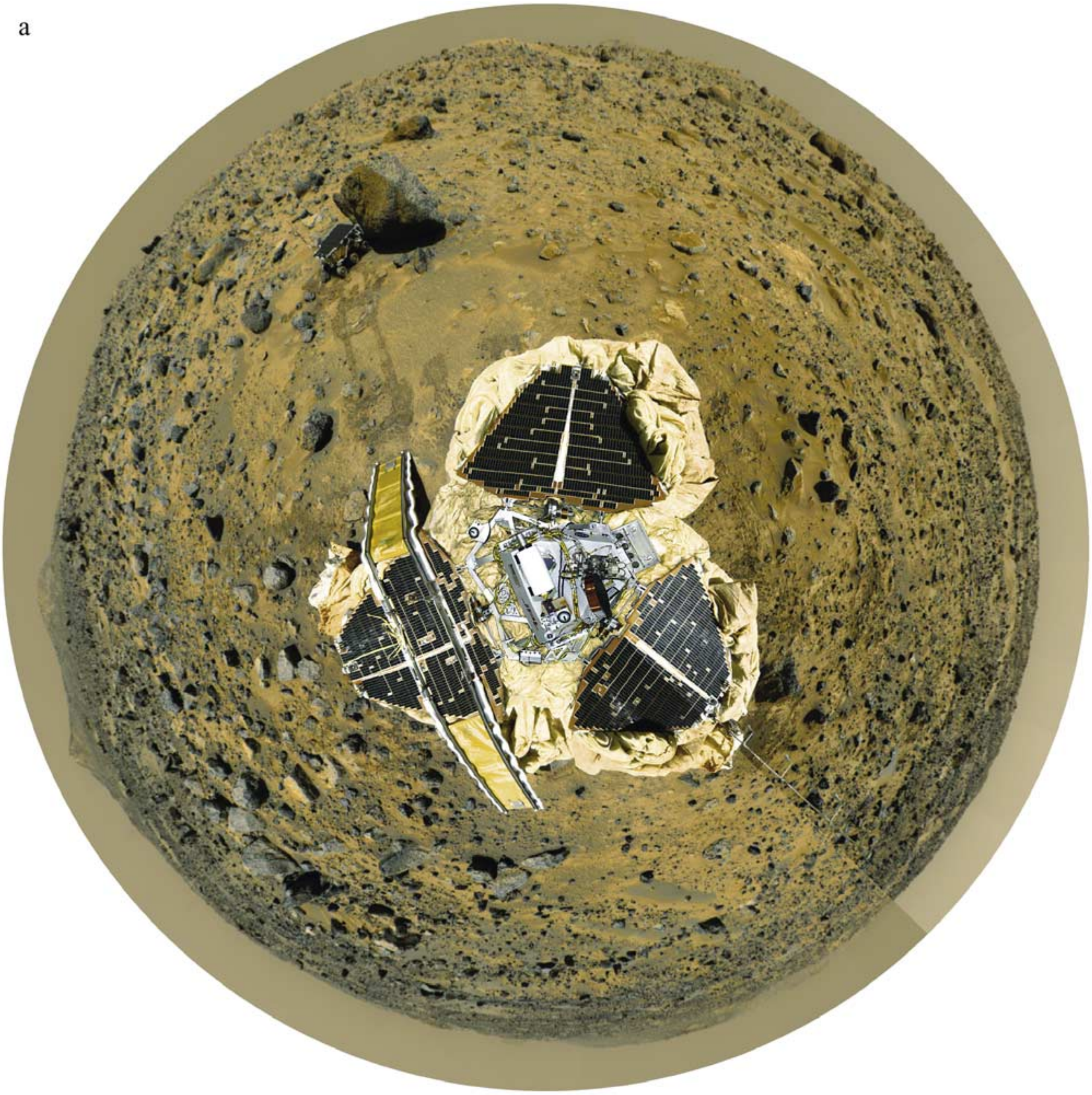

Figure 1. (a) Filled donut, or continuously cylindrical coordinate mosaic of the Mars Pathfinder landing site from the gallery panorama [*Golombek et al.*, 1999a]. Mosaic shows the lander and landing site out to the horizon in roughly the same orientation as b, so that rocks in b can be identified. North is up and west is to the left (0° to 360° clockwise). (b) Rocks (open circles scaled to rock diameter) measured at the Mars Pathfinder landing site with the showstereo software, mapped in the local level coordinate system (M-frame) in meters, which has its origin in the middle of the lander base-petal. North is up (positive LL-X). The 2.5 m to 8.5 m (dashed line) annulus is the area where the rock count was considered complete. The grayed areas are obscured regions eliminated from the counting statistics. Yogi, the largest rock in the Pathfinder near-field, is centered at (−2, 5). The Rock Garden is clearly visible by its high rock density in the southwest quadrant.

adds 1.4% to the resulting cumulative fractional area rock coverage.

2.2.2. Rock Statistics and Database Uncertainties

[7] Cumulative fractional area and cumulative number are plotted for the ShowstereoMap data set in Figures 2 and 3. Nine local-lander frame (x, y, z) locations were measured for each rock with showstereo: (1) rock position, which is the leftmost point where the rock touches the ground, (2) leftmost point on the rock, (3) rightmost point on the rock, (4) left end of rock long axis, (5) right end of rock long axis; (6) left end of rock short axis, (7) right end of rock short axis, (8) topmost point on rock, and (9) lowest

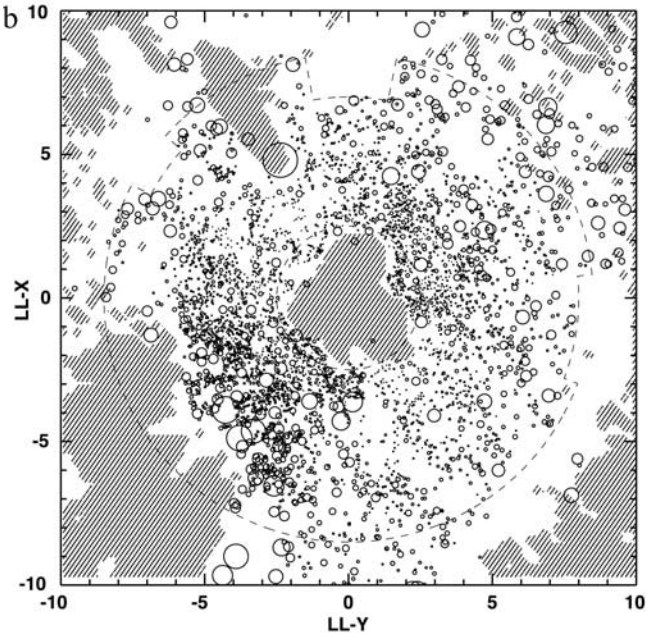

Figure 1. (continued)

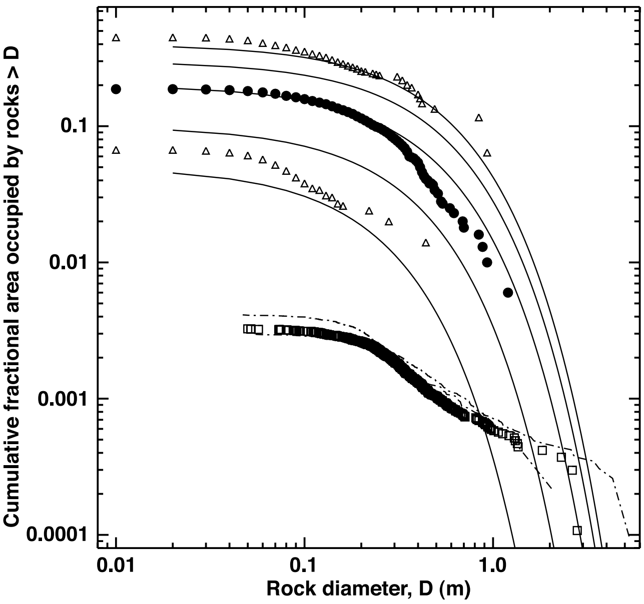

Figure 2. Cumulative fractional area covered by rocks greater than diameter D versus average rock diameter at the Pathfinder landing site. The dots are for the ShowstereoMap near-field rock count for the average (19%) distribution in the 2.5 to 8.5 m annulus in Figure 1b. Triangles are the minimum (7%) and maximum (45%) distributions measured in 45° degree segments of the annulus centered on azimuths 147.5° and 232.5°, respectively. These sample areas cover 10.5 m^2, which are comparable to the MER airbag bounce footprint. The lines are the model distributions for 5%, 10%, 20%, 30% and 40% rock coverage as derived in section 2 of this paper. The boxes show the edited far-field rocks with the dash-dotted lines showing the range of possible distributions given upper and lower range evaluations of each rock in the far-field set.

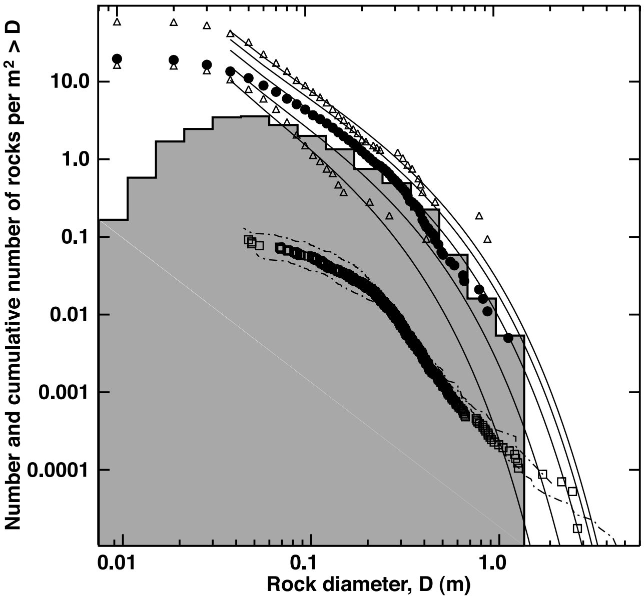

Figure 3. Cumulative number of rocks/m^2 greater than diameter D at the Pathfinder landing site. Symbols as described in Figure 2. Also plotted is the histogram of the number of rocks/m^2 present within diameter bins spaced between integer powers of $\sqrt{2}$. The histogram shows a mode at 0.5 m diameter with a steep drop in number of rocks/m^2 with increasing diameter. The mode is similar to that at VL2 and the skewed shape and long tail of the histogram (in a non log Y axis) is similar to histograms of rock diameter at VL1 and VL2.

point on rock. Average rock diameter, D, is the average of the horizontal length of the rock long axis and the horizontal length of the rock short axis [*Moore and Keller*, 1990, 1991; *Golombek and Rapp*, 1997]. It is a more correct representation of rock size than apparent width, W (the distance between leftmost and rightmost points on a rock), and D ~0.75 W as shown in Figure 4 and reported by *Golombek and Rapp* [1997]. Additionally, the ShowstereoMap manual method of picking stereo points in image pairs will have a tendency to bias both W and D high, with perhaps more bias on W. This is because of the possibility of picking a point beyond the rock for stereo matching when trying to pick the edge of a rock. Long and short axes picks on most (decimeter-sized) rocks will fall on a rock face or near the top rear of the rock rather than a tangent edge. Cases of clearly discrepant picks (i.e., that generate 5 m rocks near the lander) have of course been corrected in the ShowstereoMap database. The stereo point picking bias could also tend to flatten rocks; there is the possibility that points picked near the top of a rock may fall on the ground behind the rock generating a smaller difference between rock top and bottom. This is not likely the explanation for the general flatness of the rocks in the Pathfinder near-field as shown in Figure 5, as the rock-counters searched for the highest points and lowest points on rocks, seeking extreme z values by multiple mouse-clicks. Rocks at the Pathfinder site appear flatter than rocks at Viking Lander 1 (VL1) and 2 (VL2) with a height/diameter ratio of 0.24 versus 0.5. As will be described in section 2.3, however, far-field rocks have a higher height/diameter ratio of 0.83; averaging the

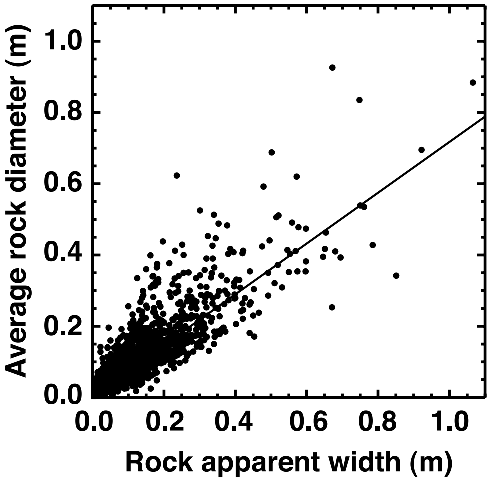

Figure 4. Plot of rock apparent width versus diameter. Best fit line suggests that the diameter of the rock is 0.71 times the apparent width of the rock. The apparent width of a rock is the total width of the rocks in silhouette, and usually includes more than one face of a rock. The actual dimensions of a rock depend on the angle at which the rock is oriented relative to the cameras. For example, for rocks oriented at 45° the apparent width will include 0.707 times the sum of the lengths of two sides, and for rocks oriented at 60° it is 0.866 times the length of one side plus 0.5 times the length of the other side. From this, *Golombek and Rapp* [1997] estimated that the diameter should be about 0.75 times the apparent width, similar to that indicated at Pathfinder.

near and far-field data yields a 0.5 height diameter ratio like VL1 and 2. Higher rocks in the far field could represent an observational bias toward recognizing taller rocks in the far field, or rocks at Pathfinder could be flatter than at VL1 and 2, consistent with the expectation of tabular (less rounded) rocks produced by the catastrophic flood [*Golombek et al.*, 1997b; *Smith et al.*, 1997].

[8] The importance of the distinction between rock apparent width and average rock diameter is most clear when we compare the ShowstereoMap results with the earlier near-field results: the older cumulative fractional areas reported are wrong. The first near-field rock count was produced using the MarsMap virtual reality software [*Stoker et al.*, 1999] during Pathfinder operations, so we call these data the "MarsMap near-field rock data set." The MarsMap virtual reality display interface relies on three dimensional models of the Martian surface that are generated from individual stereo image pairs in the Monster pan set of Imager for Mars Pathfinder (IMP) images [*Smith et al.*, 1997; *Golombek et al.*, 1999a]. The terrain model contains some minor offsets at image boundaries in the mosaic, which produces uncertainties of less than a few percent of the range for the rock position measurements [*Stoker et al.*, 1999], and less than 1 cm for the rock size. A total of 2035 rocks were measured. For each rock the (1) location in local lander coordinates, (2) rock apparent width, and (3) rock maximum height were measured. The position of the left tangent point where the rock touches the soil was chosen as the rock location, except for the first 115 rocks of the data set for which a point somewhere near the middle of the IMP-facing portion of the rock was picked. Rocks 3 cm and larger

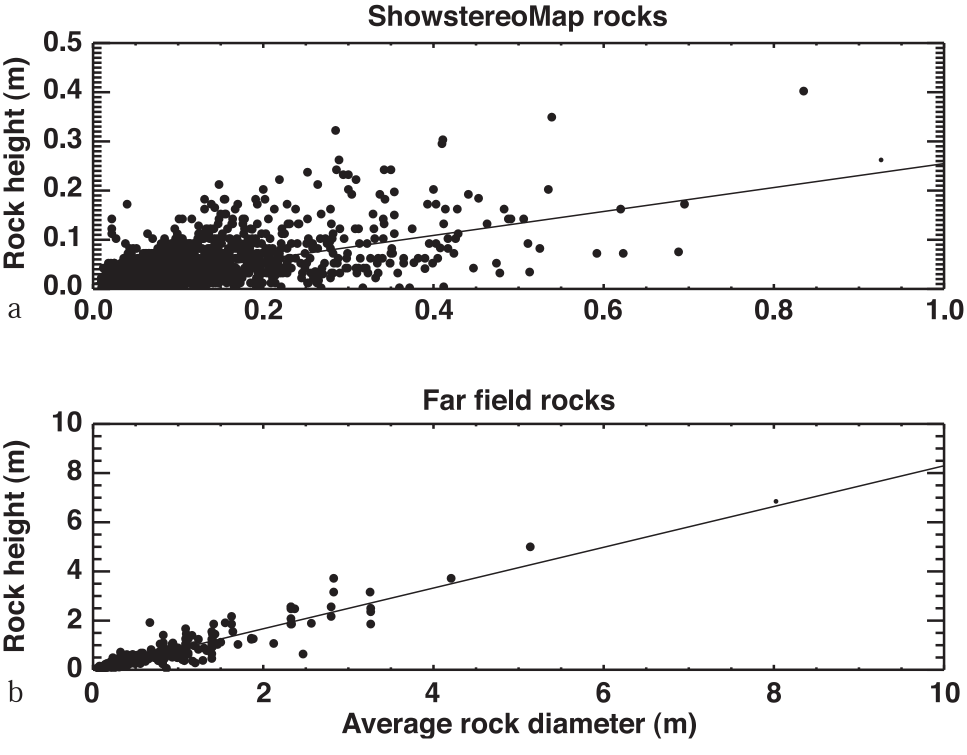

Figure 5. Plot of rock width versus rock height for the near-field data (a) and the far-field data (b). Near-field data indicate rock heights are only 0.24 times their diameter. Far-field data indicate rock heights are 0.83 times their diameter. Average rock height of both of these estimates is about 0.5, which is similar to that measured at the Viking 1 and 2 landing sites.

were thought to be thoroughly surveyed within a 3 m to 6 m annulus (1472 rocks). A map of the MarsMap rocks is given by *Golombek et al.* [1997b, Plate 5]; histograms and cumulative number and fractional area versus apparent width plots were shown by *Golombek et al.* [1997b, Plates 8, 9, and 10] and by *Golombek et al.* [1999a, Figure 2]. It is now clear that the 3 m to 6 m annulus was not thoroughly surveyed in the MarsMap database: the same annulus in the ShowstereoMap contains 2504 rocks! This difference may be due to differences in image compression of the MonsterPan and the SuperPan. The discrepancy was not discovered because (1) the difference between rock apparent width and average rock diameter was not corrected (so that the resulting area of each rock was ~75% too large) and (2) the cumulative fractional area result obtained using apparent width (16%) was so close to the predicted result and that expected from visual inspection [*Golombek et al.*, 1999a]. Given that the older data are clearly in error, they are not plotted here for comparison.

2.2.3. Cumulative Area Results

[9] The cumulative area covered by rocks within the 2.5–8.5 m annulus is shown in Figure 2, and is 18.7%, with variations ranging from 6.7% coverage in the southeastern portion of the annulus, to 44.9% coverage within the southwest quadrant. The average rock abundance is consistent with expectations prior to landing. Viking thermal differencing estimates [*Christensen*, 1986a] indicate ~20% of the surface covered by rocks >0.15 m diameter for the landing ellipse (average 20.4%, range 18–25%), with 18% for the 1° by 1° pixel containing the lander [*Golombek et al.*, 1997b, 1999a, 1999b], which is virtually identical to that measured around MPF. In section 4 we derive a slightly higher effective thermal inertia of the rock population than assumed by *Christensen* [1986a] and a similar fine component thermal inertia to that estimated [*Christensen*, 1986b] for the derived effective thermal inertia of the rock population, the rock coverage, and the bulk thermal inertia [*Golombek et al.*, 1997b, 1999b].

[10] In general, the cumulative area covered by rocks versus diameter curve is similar to the Viking 2 landing site and similar in shape to the Viking 1 landing site (without the outcrops) derived from rock counts done in a similar manner [*Moore and Keller*, 1990, 1991], with greater area covered at all diameters and with a greater variation within the area visible from the lander. A log-log plot of the data shows a clear convex up shape that is not linear (required by a power law distribution), but can be fit very well by a simple exponential function. The Pathfinder curve is very similar to the 20% model rock distribution proposed for Mars by *Golombek and Rapp* [1997]. Prior to Pathfinder landing, the VL1 and VL2 distributions were fit by equations of the form

$$F_k(D) = k \exp[-q(k)\ D], \tag{1}$$

where $F_k(D)$ is the cumulative fractional area covered by rocks of diameter D or larger, k is the total area covered by all rocks, and an exponential q(k), which governs how abruptly the area covered by rocks decreases with increasing diameter [*Golombek and Rapp*, 1997]. Similar rock distributions were also measured at a wide variety of rocky locations on the Earth [*Golombek and Rapp*, 1997] as well as more recent documentation of similar distributions in young viscous silicic flows [*Anderson et al.*, 1998] and in Hawaiian flows in various states of weathering [*Craddock et al.*, 2000]. *Golombek and Rapp* [1997] argued that the underlying cause for these exponential size-frequency distributions is fracture and fragmentation theory [e.g., *Rosin and Rammler*, 1933; *Gilvarry*, 1961; *Gilvarry and Bergstrom*, 1961], which predicts that ubiquitous flaws or joints will lead to exponentially fewer blocks with increasing size during weathering and transport [e.g., *Wohletz et al.*, 1989; *Brown and Wohletz*, 1995] (see *Golombek and Rapp* [1997] for further discussion). The VL1 and VL2 distributions specifically, were used to develop a model size-frequency distribution for Mars in which k is equal to the total rock abundance [*Christensen*, 1986a] and the exponential was approximated by

$$q(k) = 1.79 + 0.152/k. \tag{2}$$

These distributions form a family of non-crossing curves (Figure 2) that flatten out at small rock diameter at a total rock abundance of 5–40% [*Christensen*, 1986a].

[11] Prior to Mars Pathfinder landing, these model rock distribution curves were used along with the thermal estimate of rock coverage [*Christensen*, 1986a] to predict the surface area covered by large potentially hazardous rocks to the Pathfinder airbags. The distribution of rocks measured at the Mars Pathfinder landing site generally follows the model distribution for total rock abundance of 20% (Figure 2). The maximum reached at small diameters is the total rock coverage (20%) and the area covered by 1 m diameter boulders is 1%, which is as predicted prior to landing using the model distributions [*Golombek and Rapp*, 1997; *Golombek et al.*, 1997a].

[12] The Pathfinder cumulative area distribution deviates from the model distribution in a few areas. The cumulative area covered by rocks with diameters between 0.4–0.8 m is less than the model. Below 0.4 m diameter, the Pathfinder cumulative area distribution tracks the model distribution quite well (Figure 2). At diameters above 0.9 m the MPF cumulative area covered by rocks is 2–3% lower than the model for 20% rock abundance. As will be illustrated in section 3, the MPF cumulative area distribution is generally similar to the VL2 cumulative area distribution except that the MPF cumulative area distribution slightly exceeds VL2 at diameters >0.8 m and <0.35 m and is slightly less than VL2 in between. The minimum and maximum area distributions measured from the Mars Pathfinder lander also generally track the model distributions for 7% and 45% rock coverage, although the measured distributions are a few percent low between diameters of 0.3–0.07 m.

2.2.4. Cumulative Number Results

[13] The cumulative number of rocks at the Pathfinder site is generally similar to the Viking 2 landing site and similar in shape to the Viking 1 landing site, with more rocks at all diameters except for 0.4–0.8 m. When plotted as the cumulative number of rocks per meter squared versus diameter on a log-log plot (Figure 3), the shape of the distribution is generally convex up and similar to many rocky sites on Earth [*Golombek and Rapp*, 1997]. At diameters between 0.05 and 0.4 m, the distribution can be approximated reasonably well by a straight line, which is

similar to power law behavior [*Moore and Jakosky*, 1989; *Moore and Keller*, 1990, 1991], with 0.3 to 10 cumulative number of rocks/m^2. Below 0.2 m diameter, the cumulative number of rocks/m^2 at the MPF landing site exceeds that at the VL2 landing site by a factor of 2 to 4, with a total of just under 20 rocks/m^2. At all three landing sites, the distribution of rocks above 0.8 m diameter and below 0.2 m diameter is not approximated by the power law distribution fit to the rocks in between. At small diameters, the distribution flattens out and reaches a maximum (the total number of rocks/m^2); at large diameters the distribution drops off more rapidly than the power law defined for the distribution in the 0.2–0.8 m diameter range. In between, the cumulative number and cumulative area distributions (particularly the minimum) show portions with distinct slopes (Figures 2 and 3). Rocks between 0.8 and 0.5 m, 0.5 to 0.3 m, and 0.3 to 0.08 m diameter have distinct slopes that in some cases appear as straight lines suggestive of various power law distributions. The cause of these breaks in slope could be due to different processes active at different diameter ranges as suggested by *Malin* [1989] and proposed at the Pathfinder site (small angular ejecta versus semi-rounded tabular boulders carried by the flood) [*Golombek et al.*, 1997b].

[14] A reason the Mars Pathfinder site contains so many more rocks <0.2 m diameter than the Viking sites may be the geologic setting in which remote sensing data suggested a less dusty environment than Viking 1 and 2 [*Golombek et al.*, 1997a, 1999b; *Bell et al.*, 2000] and interpretations of the surface around the Pathfinder lander suggest a region of net erosion or loss of material [*Greeley et al.*, 1999, 2000; *Ward et al.*, 1999; *Golombek and Bridges*, 2000].

[15] One of the difficulties of using these model size-frequency distributions is that they were cast in terms of the cumulative area covered by rocks greater than a given diameter versus diameter (equation (1)) and many engineering applications prefer the cumulative *number* of rocks greater than a given diameter versus diameter [e.g., *Bernard and Golombek*, 2001]. The simplest method for generating cumulative number distributions for a given rock abundance that is identical to the cumulative area distribution is to numerically integrate the cumulative area curves. This is illustrated in Figure 3, which plots the cumulative number of rocks per square meter of a given diameter or larger versus diameter for model rock distributions and data from the three landing sites on Mars. Model rock distributions for 5%, 10%, 20%, 30% and 40% total area covered by rocks were derived by numerically integrating the cumulative area function (equation (1)) in small diameter increments.

[16] As can be seen from Figure 3, the simple numerical integration of the cumulative area function fits the observed rock distributions at Mars Pathfinder quite well for diameters greater than 0.1 m. The total number of rocks should reach a maximum at diameters near 1 cm (see discussion by *Golombek and Rapp* [1997] and *Malin* [1988, 1989]), but the model curves derived in this manner do not. The reason the curves do not reach a maximum is that they are not actually exponentials. *Golombek and Rapp* [1997] show that going from the cumulative number versus diameter distributions to the cumulative area versus diameter distributions in a mathematically rigorous way actually introduces a quadratic equation into the relationship [see *Golombek and Rapp*, 1997, equations (5)–(10)]. Because of this, simply taking the cumulative number relations and determining the number of rocks in small diameter bins and multiplying the number of rocks of a given size by the area of a rock of this size will underestimate the area covered by rocks of that size. There is no analytic way to go from the cumulative area relationship to a cumulative number relationship (a difficulty of using exponential functions over simple power law relationships proposed previously; see discussion by *Golombek and Rapp* [1997]). For our analysis, we will use these numerically integrated model curves for rock diameters greater than 0.1 m diameter for deriving the number of rocks of a given size or larger for areas of different total fractional rock coverage. The discrepancy below 0.1 m diameter can be ignored in this analysis because in this paper we are concerned with rocks larger than this.

[17] As for the cumulative area distributions at the Mars Pathfinder site, the maximum and minimum cumulative number distributions also generally track the model distributions. The maximum distribution at the Pathfinder site (45% area covered) generally falls along the 40% model distribution, except for the largest 2 diameter bins. The minimum distribution at the Pathfinder site (7% area covered) generally falls between the 5% and 10% model curves (Figure 3).

2.3. Far-Field Measurements

2.3.1. Method

[18] Far-field rocks were measured using the stereo baseline afforded by the IMP camera mast, separated by 0.85 m height before and after deployment, using two different methods, which were then combined. In the first method, the "horizon method," the difference in pixel distance of far-field rocks to the horizon between pre- and post-mast deploy images determines the rock range. The range then determines the apparent width of the rock, which can be related to the diameter (average of the length and width) [e.g., *Golombek and Rapp*, 1997]. This method was used during Pathfinder operations, and the results constitute the far-field points in Figures 2 and 3 of *Golombek et al.* [1999b]. The follow-on far-field rock count which we report here, began with this same method, tagging some 961 far-field rocks in deployed-mast images, and finding that 462 of these could also be observed in the pre-deploy images. A minimum rock width of 5 pixels was used. This selection factor determines the maximum range at which rocks of a given size can be identified. In the second method, rock ranges are triangulated using IMP pointing information for images collected from the stowed (Insurance Pan) and deployed (Super and Gallery Pans) camera positions (in the lander frame coordinate system). This "triangulation method" yielded a maximum viewing distance of 620 m and a minimum apparent width of a rock at that distance of 3.1 m. Approximately 1 km^2 area was studied, consisting of a circle of radius 620 m with some areas obscured due to lander obstructions and large, near-field rocks. For each of the 462 rocks, the horizon method ranges and the triangulation method ranges were compared among adjacent rocks in the same images or adjacent images. The apparent relative ranges of those rocks together were used to generate a hand-edited list of far-field rock ranges with a maximum rock range of 250 m. Calculations of cumulative fractional

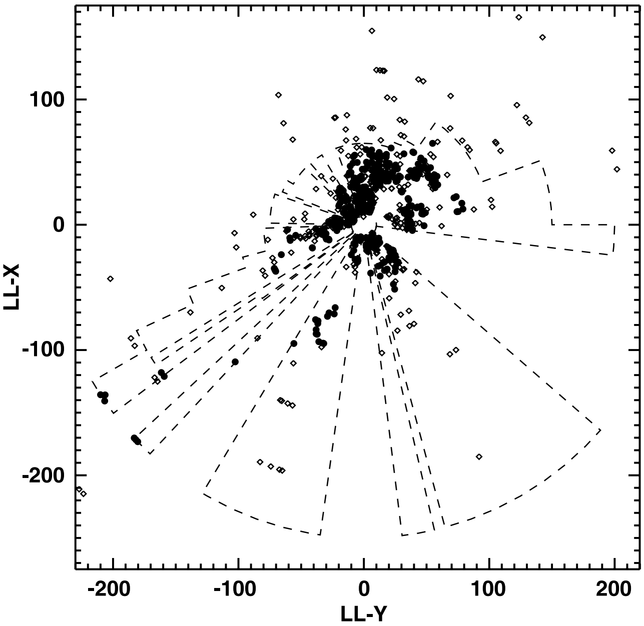

Figure 6. Map of far-field rock locations in lander coordinate frame (L-frame) in meters derived via the method described in the text. The dashed lines outline the outer and inner boundaries of the area considered unobscured for discovery of large rocks in the far field. The open crosses show locations determined by the horizon method alone. The black dots are the edited far-field rock locations that include pre- and post-deploy IMP image triangulation along with edits based on visual inspection.

area and cumulative number are normalized to an area (0.057 km^2) extending to the rock's range, but also account for near-field obscurations (see Figure 6).

2.3.2. Cumulative Area Results

[19] The area covered by rocks larger that 1 m, shown in Figure 2 is low (0.06%) and decreases below 0.01% at diameters above 3 m. These values are 5–10 times smaller than those derived from a crude count of large rocks in the far field [*Golombek et al.*, 1999b]. Although the shape of the far-field curve deviates from the near-field distribution, the area covered by rocks greater than 2.5 m in diameter fits very well with that predicted at these large diameters by the exponential fit to the near-field data [see also *Golombek et al.*, 1999b]. A reasonable explanation for the lower slope in the smaller diameter rock far-field data may be a resolution effect (similar to counting craters near the limit of resolution of an image), where fewer rocks of a given size are counted than are actually there. This would produce fewer rocks at progressively smaller sizes than are actually there (a similar effect can be seen in the far-field measurements of the Viking 1 landing site [*Golombek and Rapp*, 1997]). In addition, we have not accounted for obscuration effects that would decrease the number of rocks recognized in the far field. An alternative to this is that there may be multiple segments to the rock distribution curves [e.g., *Malin*, 1988, 1989]. Even if the area of the far-field estimate is off by an order of magnitude or the difference in the shape of the distributions at the large diameters is real, the area covered by large rocks is orders of magnitude smaller than suggested by power law fits to the smaller diameter near-field rocks. This result further supports the use of exponential functions for estimating rock size-frequency distributions for engineering studies of potentially hazardous blocks on the surface of Mars. In addition, these results further confirm the pre-landing prediction for the cumulative area covered by large, potentially hazardous rocks at the Mars Pathfinder landing site [e.g., *Golombek et al.*, 1997a, 1999b].

2.3.3. Cumulative Number Results

[20] The far-field data statistics, shown in Figure 3 cover a much larger area than the near-field and so is less subject to the problem of having one large rock in a small counting area. The far-field results show that the cumulative number of rocks/m^2 greater than 2 m diameter is 2 orders of magnitude smaller than the near-field data for rocks >1 m diameter or roughly 0.00008/m^2. Although the shape of the curve defined by the far-field rocks is different than the near field (probably due to the resolution effect described earlier), the number of rocks at large diameter is clearly lower than described by a power law fit to the 0.2–0.8 m diameter rocks and is generally consistent with the numerically derived model for 20% rock coverage derived from the near-field cumulative area data.

3. Extreme Rock Distributions on Mars

3.1. MOC Boulder Fields

[21] As a further test of these model rock distributions and the distribution of very large rocks on Mars in general, a survey of the first 30,000 released high-resolution MOC images [*Malin et al.*, 1998] revealed roughly a few percent with fields of boulders. Large and dense boulder fields (with hundreds to thousands of boulders) were typically at the base of scarps or around fresh craters [e.g., *Malin and Edgett*, 2001] and were found in a fraction of one percent of MOC images, typically with low Sun angle. Boulders around two ~500 m diameter relatively fresh impact craters (MOC images M02-01741 and M03-00265), three relatively fresh grabens (M03-06759, M02-02352, and M02-02582), and the caldera scarps of Olympus Mons (M04-02248) were counted. The total area surveyed in each MOC image was typically about 10 km^2 (0.6–14 km^2). Three to five subareas in each image were tabulated; over 14,000 boulders were counted in all 6 images. In addition, all MOC images in and around the final 4 MER landing sites were searched for boulder fields. A total of 143 MOC images of the landing sites uncovered 14, 10, 3, and 0 boulder fields in Gusev, Isidis, Elysium and Meridiani, respectively. Counts were made of 8 boulder fields in 6 MOC images in the Gusev landing site area (E17-01547, E17-00827, E13-01593, E18-01498, E03-00012 and E11-02024). A total of 1134 boulders (53–479 per field) with diameters from 2 to 15 m were counted over areas of 0.03–3.2 km^2. Of these, only one, near the eastern end of the Gusev landing ellipse (E18-01498), is comparable in area and number of boulders to the other areas found in the survey (above). All of the other boulder fields are smaller (in area and number of boulders) and are associated with craters. An example is shown in Figure 7, which shows a ~340 m diameter relatively fresh impact crater with some fresh crater rays. The inside of the crater has a series of sand dunes in it, the rim has a rounded appearance, and the

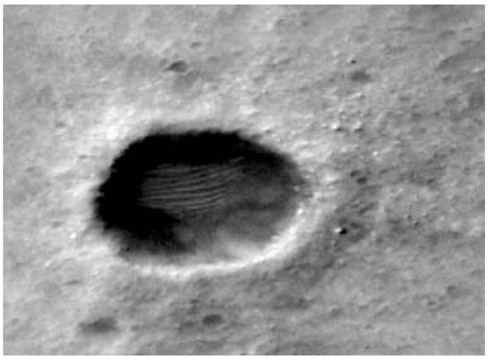

Figure 7. Relatively fresh ~340 m diameter impact crater in the Gusev landing ellipse in MOC image E03-00012 (Sun angle 49°) in which boulders were counted. A total of 77 boulders were counted with diameters from 4 m (the pixel resolution of the image) to 12 m. The maximum boulder concentrations are from the northeastern quadrant of the ejecta field (north is up).

surface to the southeast of the crater lacks fresh ejecta, all of which suggest the crater has undergone some degradation. This is among the freshest of the impact craters with associated boulder fields, so that most of these surfaces are the remains of a modified surface that has been subjected to erosion and/or deposition. A portion of the Olympus Mons caldera scarp and a portion of the Gusev MER landing ellipse [*Golombek et al.*, 2003] in which boulders were counted are shown in Figures 8 and 9.

[22] Boulders were fairly easy to identify as pairs of light and dark pixels (bright and shaded sides) on the images. The diameter was simply the number of pixels across measured perpendicular to the Sun azimuth (along the line between the light and dark pixels), scaled for the image resolution, emission angle, and angle of the perpendicular to the Sun azimuth relative to the pixel grid. In practice, boulders down to one pixel diameter could be measured as a light and dark pixel pair. Although there was some uncertainty in the identification, it was generally repeatable, with different observers yielding similar results. Measured boulder diameter is probably within ±1 pixel. The smallest diameter boulder measured was about 1.5 m and the largest was just over 20 m.

[23] Of all the boulder fields counted, the representative subareas with maximum concentrations are shown in Figures 10 and 11, which include the graben floors, the Olympus Mons caldera scarps, and the fresh crater (Figure 7) and field near the Gusev ellipse (Figure 9). In general, the average and minimum rock distributions in the boulder fields are a factor of 2–5 and 10 smaller, respectively, than the maxima, and have a similar shape and so overlap the model distributions. These distributions can be considered representative of the maximum boulder distributions measured. Of these maximum distributions, the fresh crater and field near the Gusev ellipse shown are the maximum and minimum for the boulder fields counted near the landing site ellipses.

[24] All of the fields have boulders 10 m in diameter or larger, with 0.1–4% area covered by boulders >5 m in diameter, 0.01–3% area covered by boulders >10 m in diameter, and <0.01% area covered by boulders $\geq$20 m diameter (Figure 10). The rockiest portion of the relatively fresh impact crater in the Gusev landing ellipse has about 4% of its surface covered by >5 m diameter rocks. All of the boulder fields near the Gusev landing ellipse area fall between this maximum and the minimum near the eastern end of the ellipse. Even though these distributions are up to an order of magnitude greater than the model rock distributions, the shape of the distributions are generally parallel to the model distributions showing the steep decrease in area with increasing diameter. The flattening of the distributions at small diameter is probably a resolution effect, but even so, it is not clear what happens to these extreme distributions at smaller diameter. It is unlikely that the number of small rocks continues parallel to the model distributions, because the total area covered by rocks would exceed 100% (the maximum). More likely, the distributions flatten out at smaller diameters or even are composed of multiple branches or segments [e.g., *Malin*, 1988, 1989]. Although such large distributions are not observed in thermal differencing measurements at larger spatial scales observed from orbit (down to 3 km pixels [*Christensen*, 1986a] or smaller in TES (Thermal Emission Spectrometer) [*Nowicki and Christensen*, 1999]), they could exist on smaller spatial scales. For reference, the maximum distribution of large rocks (>1 m diameter) seen from a lander, on the rim of a crater in the far field of VL1, is elevated above

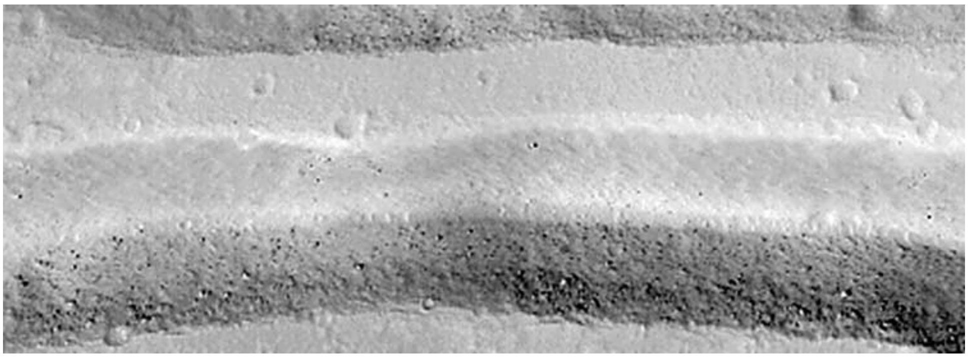

Figure 8. Boulder field on Olympus Mons caldera scarp. This area has the highest concentration of boulders of 5 regions counted within this image. A total of 1183 boulders were counted with diameters from 6 m to 24 m. Portion of MOC image M04-02248 (3.04 km wide) at 6 m/pixel resolution and Sun angle of 45°.

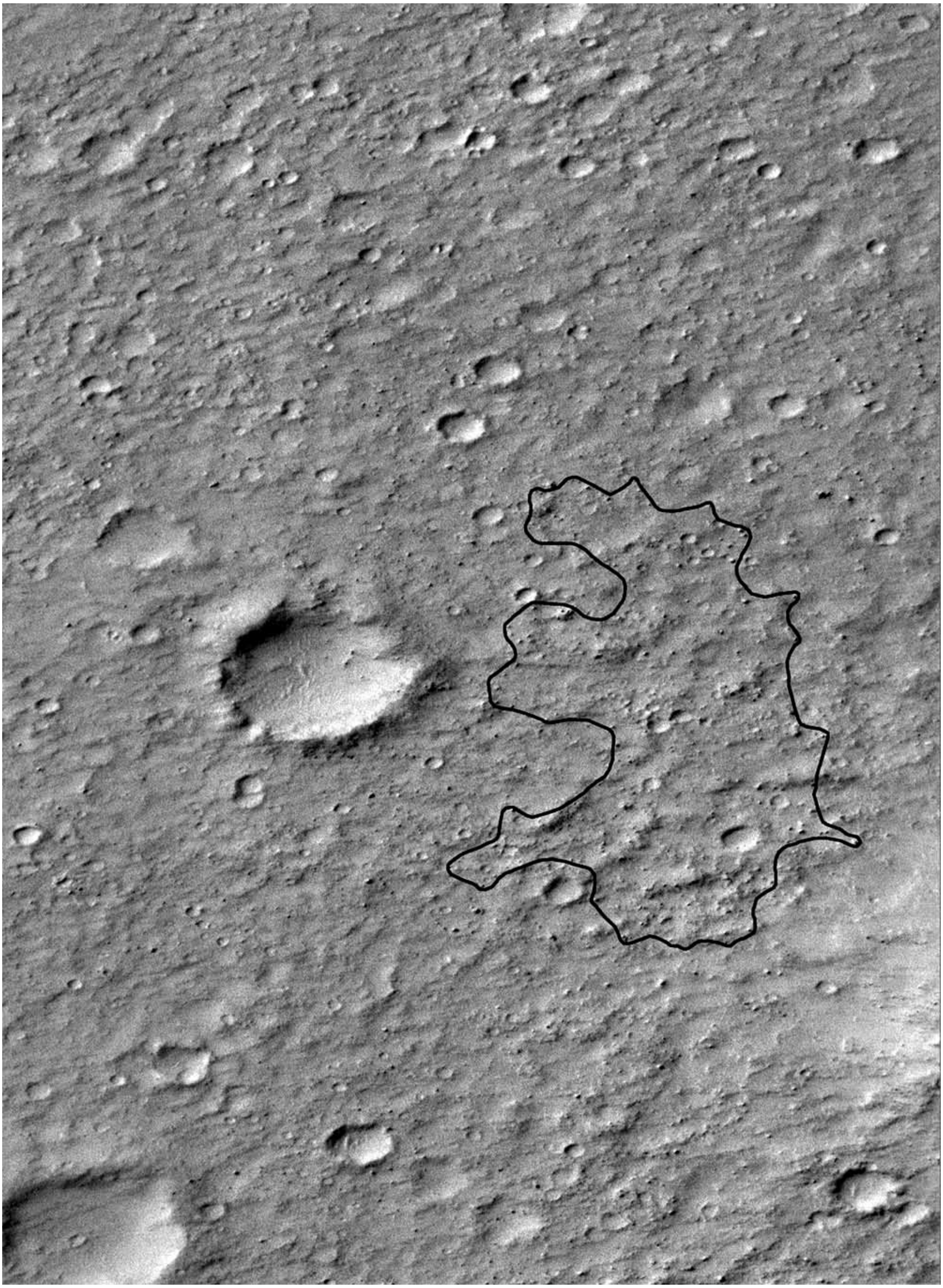

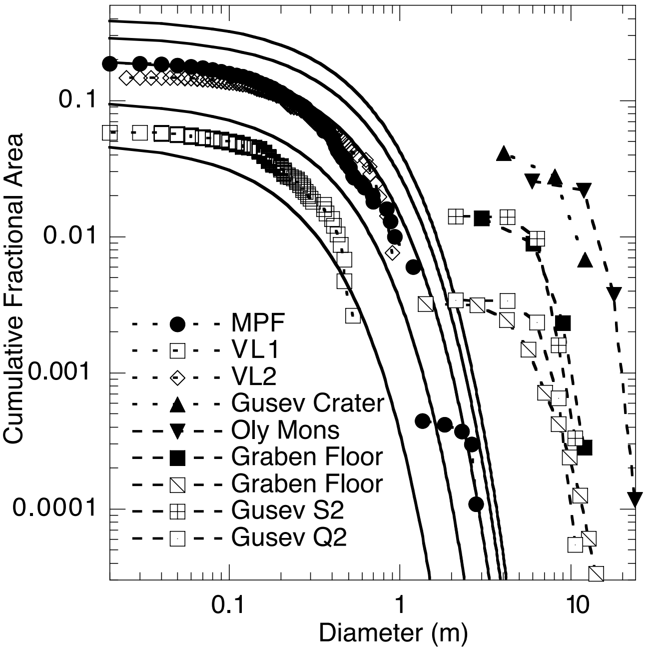

Figure 10. Cumulative fractional area versus diameter plot of the VL1, VL2, and MPF landing sites, model rock distributions for Mars, and boulder fields measured in MOC images. The model rock distributions for 5%, 10%, 20%, 30% and 40% are shown as solid lines (distinguishable by where they intersect the Y axis). Rock distributions measured from the near field of VL1 and VL2, and the near and far field of MPF are shown as a symbol for each rock or rock diameter. The maximum rock distributions measured in a sample of the boulder fields are shown, with a symbol for each rock diameter and dashed connecting lines. The crater is from a relatively fresh ~340 m diameter crater in the Gusev landing ellipse in MOC image E03-00012 shown in Figure 7. The Olympus Mons caldera scarp is from MOC image M04-02248 shown in Figure 8. The graben floors are in MOC images M02-02582 (greater rock coverage) and M02-02352 (less rock coverage). Gusev crater are for Quadrant 2 (Q2) and Sample Area 2 (S2) in MOC image E18-01498 (Figure 9).

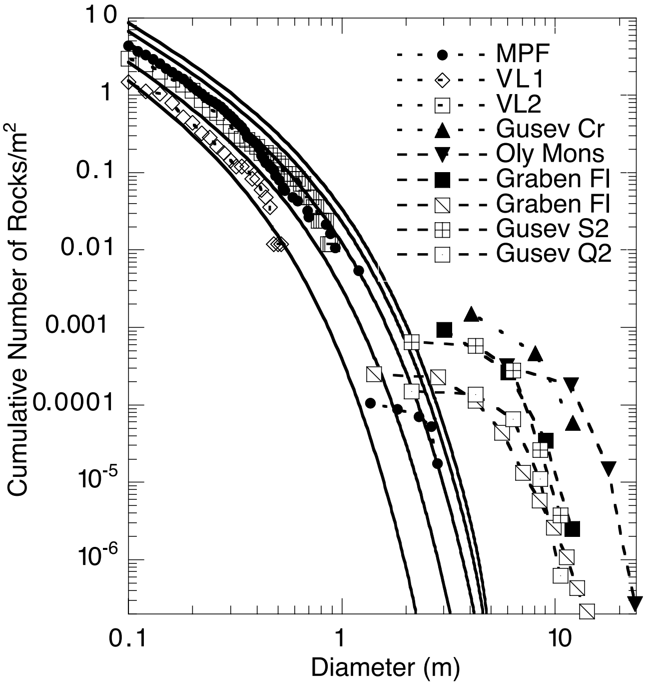

Figure 11. Cumulative number of rocks/m^2 versus diameter of the VL1, VL2, and MPF landing sites, model rock distributions for Mars, and rare boulder fields measured in MOC images. The model rock distributions for 5%, 10%, 20%, 30% and 40% are shown as solid lines. Rock distributions measured from the near field of VL1 and VL2, and the near and far field of MPF are shown as a symbol for each rock or rock diameter. Others as described in Figure 10.

that found in the near field [*Golombek and Rapp*, 1997], but falls along the 20% model distributions at these diameters.

[25] These boulder counts appear to represent the maximum distributions likely to be encountered on Mars. Fits to the cumulative fractional area versus diameter distributions result in best fits to k and q(k) in equation (1), where k is the total area covered by all rocks and q(k) controls how quickly the area covered by rocks decreases with increasing diameter. The model rock distributions from VL1 and 2 yield q(k) that varies between 5 and 2 according to equation (2) for total rock abundances, k of 5–40%. Curves displaced to the right of the model distributions (Figure 10) have smaller q(k), whereas those displaced to the left have larger q(k). Fits to a wide variety of very rocky surfaces on the Earth [*Golombek and Rapp*, 1997; *Anderson et al.*, 1998; *Craddock et al.*, 2000] show that the sites with the largest boulders (and typically the largest k) have q(k) much less than 1. As a result, these populations of boulders represent the greatest cumulative area and largest primary blocks for the process that produced or emplaced them [e.g., *Anderson et al.*, 1998]. The size of the largest block can then be inferred to represent the maximum available due to ubiquitous flaws or joints that will lead to exponentially fewer blocks with increasing size during weathering and transport (see discussion by *Golombek and Rapp* [1997], *Rosin and Rammler* [1933], *Gilvarry* [1961], *Gilvarry and Bergstrom* [1961], *Wohletz et al.* [1989], and *Brown and Wohletz* [1995]). As a result, these boulder fields can be used to probe the largest ejecta block to be transported intact by impact events of different sizes, the largest block to be transported intact by a flood, or the frequency of joints and

---

Figure 9. (opposite) Portion of boulder field near the eastern end of the Gusev landing ellipse (inside Thira crater) with high concentration of boulders (Quadrant 2 or Q2). A total of 479 boulders 2.1 m to 10.6 m diameter were measured (3.2 km^2 area). Outlined area (Sample Area 2 or S2) has the highest concentration of boulders in the area, in which 174 boulders 2.1 m to 10.6 m diameter were measured (0.27 km^2 area). Crater to west of outlined area is 300 m in diameter. Note the rounded rim and material deposited in the interior indicating the crater is not fresh. Portion of MOC image E18-01498 is 1.5 m/pixel resolution, uncorrected for emission angle. North is up.

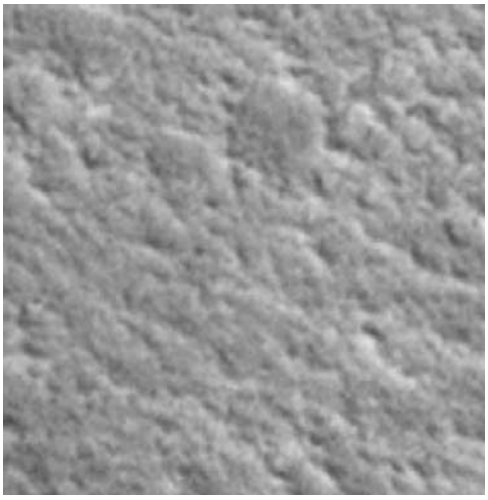

Figure 12. Highest-resolution (1.58 m/pixel) MOC image M11-02414 of the Mars Pathfinder landing site (Sun angle 48°). At most a couple of boulders might be recognizable in the image (about 330 m wide).

cohesion of the rocks being mechanically weathered in fault scarps of grabens and calderas.

[26] The plots of cumulative number of rocks per square meter versus diameter for the VL1, VL2 and MPF landing sites and the boulder fields are shown in Figure 11. These distributions can also be fit with exponential functions with noticeable curvature to the distributions at large and small diameters (on a log-log plot), but with more linear distributions at intermediate diameters. For the VL1, VL2 and MPF landing sites, less than 0.01/m^2 rocks $\geq$1 m diameter are present. For the boulder fields, 0.00004–0.0015/m^2 rocks $\geq$5 meters diameter are present, and 10^{-6}–10^{-3}/m^2 rocks $\geq$10 meters diameter. The maximum concentration of boulders near the relatively fresh crater and the eastern boulder field at the Gusev site are 0.0015 and 0.001 rocks/m^2 $\geq$4 m diameter, respectively, which represent the maximum and minimum for all the boulder fields counted.

3.2. Comparison to Landing Sites

[27] These extreme rock distributions must be compared with those observed at the VL1, VL2 and MPF landing sites to be placed in perspective. All three landing sites fall within the rockiest 15% of the planet [*Christensen*, 1986a]. In thermal measurements and surface rock counts [*Golombek and Rapp*, 1997; *Christensen*, 1986a; *Golombek et al.*, 1997b, 1999b9], the three landing sites have total rock abundances of 15–20%, yet have <1% of their surfaces covered by rocks >1 m diameter. Furthermore, the highest resolution MOC images of the landing sites (1.5 m/pixel) show at most one or two rocks in the entire imaged areas [*Malin and Edgett*, 2001], which cover tens of square kilometers. This particularly appears to be the case for the Mars Pathfinder landing site in which boulders are difficult to discern in the highest resolution MOC image (Figure 12), even though over 10 rocks >1 m diameter can be seen from the lander (e.g., Figure 13). This suggests 10^{-5}–10^{-6}/m^2 rocks greater than a few meters diameter, which is consistent with extrapolations to these diameters from the measured populations at the landing sites and areas covered by these large rocks of thousandths of a percent.

[28] For reference, the MPF and MER airbag systems have been successfully tested against surfaces with $\geq$10% area covered by rocks 1 m in diameter [*Golombek et al.*, 1997a] (section 5 of this paper). The airbag stroke is around 1 m and they withstood repeated impacts against multiple 0.5 m high rocks during testing. Rocks greater than 1 m diameter have been considered potentially hazardous, for typical height to diameter ratios of 0.5. The landing site constraint for MPF and the preliminary constraint for MER is $\leq$1% of the area be covered by rocks >0.5 m high. Note that the reconstruction of the Pathfinder landing indicates the lander bounced more than 15 times traversing about

Figure 13. Boulders seen from the Mars Pathfinder lander. Rover is adjacent to Yogi, which is over 1 m in diameter. Large rock on the left horizon is Couch, which is also over 1 m in diameter. Large rocks are obviously present at the landing site, but are difficult to recognize in the high-resolution MOC images. Portion of the gallery panorama looking northwest.

1 km [*Golombek et al.*, 1999a]. Airbag testing against a tilted platform showed the total impact area to be about 15 m^2. If the lander bounced 15–20 times, a total area of 195–260 m^2 was sampled. For cumulative number 0.01/m^2 rocks $\geq$1 m diameter measured at Pathfinder, 2–3 rocks of this size were likely encountered without damage during landing. This comparison of MOC images with rare fields of hundreds to thousands of boulders 2–20 m in diameter to the three landing sites, where such boulders are virtually absent, suggests that most of Mars where boulders cannot be seen is relatively free of large rocks and thus safe for landing MPF.

4. Thermal Inertia of Rocks and Rock Populations

4.1. Effective Thermal Inertia of Rocks

[29] In this section of the paper, we explore the effective thermal inertia of rocks and rock populations, interpret the results in terms of abundances and populations of potentially hazardous rocks, and conclude with interpretations of rock hazards on the Martian surface and in high thermal inertia areas found by TES. Spectral differencing of thermal measurements of Mars from the Viking Infrared Thermal Mapper (IRTM) have been used to derive the rock component of a two component surface for an assumed effective thermal inertia of rocks [*Christensen*, 1986a]. These estimates typically assume an effective thermal inertia of about 1250 (J m^{-2} $s^{-0.5}$ K^{-1} or SI units) for rocks of diameter 0.1–0.15 m [*Kieffer et al.*, 1973, 1977; *Christensen*, 1982, 19876a]. In a review of thermal inertia data versus particle size, *Jakosky* [1986] found that rocks greater than 0.2 m in diameter should have an effective thermal inertia approaching 2500, whereas particles of 0.001 to 0.03 m size should have effective thermal inertias of about 400. To derive the effective thermal inertia of a rock population we applied a simple empirical model of effective inertia versus rock diameter that is consistent with these estimates. This model assumes that rocks with diameters greater than 0.26 m have inertias of ~2100, rocks with diameters 0.01–0.03 m have inertias of 420 and rocks in between have inertias that vary as the 0.75 power of their diameter [*Golombek et al.*, 1999b] (Figure 14). This model simplifies a number of effects, such as the real variation of rock temperature with look direction (i.e., observing the hotter versus colder part of a rock [*Jakosky et al.*, 1990]). In addition, the model is for surfaces with discrete rocks in a lower fine-component background inertia unit and is not applicable to surfaces with bulk inertias greater than ~800, including bare rock surfaces with bulk thermal inertias of ~2200 discovered by THEMIS (Thermal Emission Imaging System) [*Christensen et al.*, 2003].

[30] The effective thermal inertia for the entire rock population is calculated in this model by summing the products of the thermal inertias and areas for each rock and dividing by the total area covered by all the rocks. This calculation is thus most sensitive to the shape of the cumulative fractional area versus diameter distribution of rocks and not the total area covered (which is normalized out) or to the exact values of the effective rock inertia, which are accommodated later in the model. For the cumulative fractional area of rock versus diameter model distributions discussed earlier, this parameter is the exponential factor, q(k) in equation (1), which governs how abruptly the area covered by rocks drops off with increasing diameter.

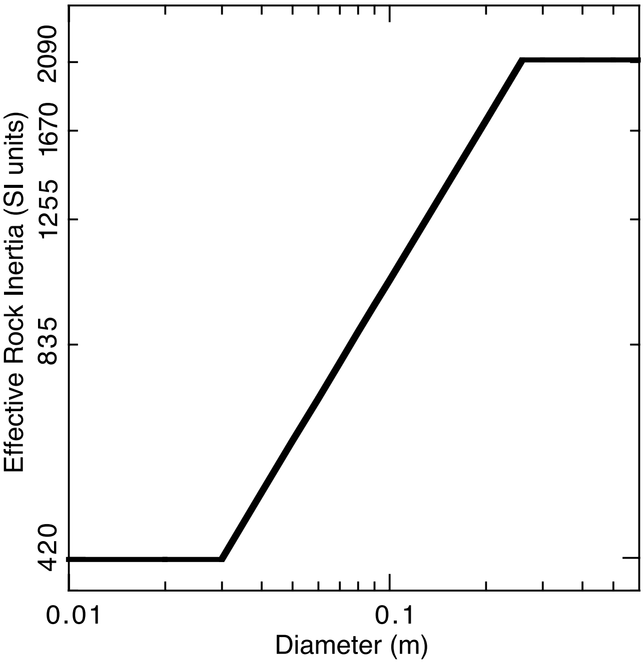

Figure 14. Effective rock thermal inertia in SI units or J m^{-2} $s^{-0.5}$ K^{-1} versus diameter derived from simple empirical model used by *Golombek et al.* [1997b, 1999b] based on thermal inertia versus particle size review by *Jakosky* [1986] and other references discussed in text. This model assumes that rocks with diameters greater than 0.26 m have inertias of ~2100, rocks with diameters 0.01–0.03 m have inertias of 420 and rocks in between have inertias that vary as the 0.75 power of their diameter. Results using this model are not sensitive to the exact effective inertia assumed for a particular particle size and uncertainties are accommodated later in the model.

4.2. Effective Thermal Inertia of Rock Populations

[31] Applying this equation to rock distributions on Mars and Earth analog sites shows that the total effective rock inertia typically covers a narrow range of 1700–2100 (Figure 15). For measured rock distributions at the VL1, VL2 and MPF landing sites, the total effective thermal inertia of the rock populations are 1700 for Pathfinder and 1900 for the Viking sites (without outcrops Viking 1 yields 1700). Most Earth analog sites reported by *Golombek and Rapp* [1997] show a similar total effective thermal inertia of 1700–2100 for the measured rock distributions. The cumulative fractional effective rock inertia versus diameter plots generally mimic the cumulative fractional area versus diameter plots and are consistent with simple exponential functions in which the pre-exponential factor is the effective inertia of the entire rock population, and the exponential factor controls the decrease with increasing diameter.

[32] Rock size-frequency distributions with gradual drop off in cumulative area with large diameter (such as the Ephrata Fan distribution), similarly show relatively flat

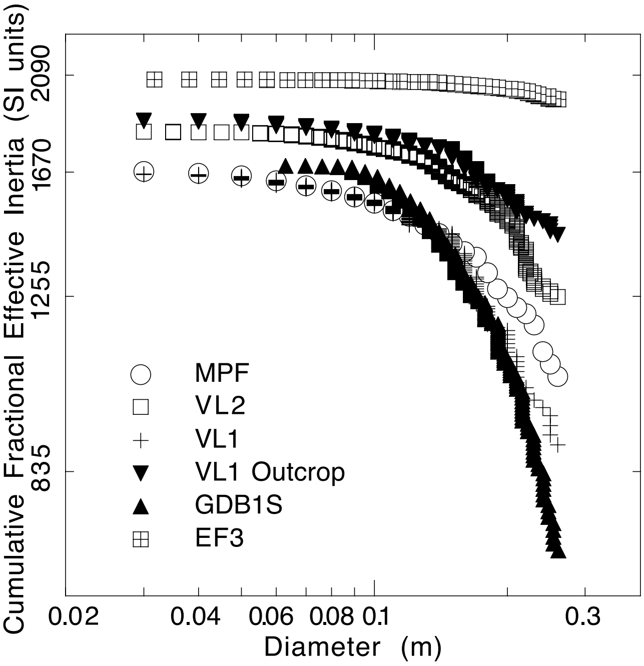

Figure 15. Cumulative fractional effective thermal inertia versus diameter of measured rock populations on Earth and Mars. Mars Pathfinder (MPF), Viking 1 with outcrops (VL1 Outcrop) and without outcrops (VL1), Viking 2 (VL2), a weathered Miocene basalt surface in Goldstone (GLDB1S) and the Ephrata Fan (EF3) all show that the total cumulative effective inertia of natural rock populations with diameter >0.03 m are between 1650 and 2100. The shape of the curves is governed by the exponential factor q(k) which controls how rapidly the cumulative fractional area curves decrease with increasing diameter (equation (1)) and not the exact values of the effective rock inertia. Data for the Goldstone and Ephrata Fan surfaces are described by *Golombek and Rapp* [1997].

cumulative fractional effective inertia versus diameter plots in which the cumulative fractional inertia of rocks greater than 0.26 m in diameter is 90% of the total (Figure 15). The other extreme is found in rock distributions with an abrupt decrease in cumulative fractional area with increasing diameter that have larger q(k) such as Mars Hill in Death Valley or the Goldstone basalt surfaces in the Mojave Desert [see *Golombek and Rapp*, 1997], in which less than half the cumulative fractional effective inertia is produced by rocks of diameter greater than 0.26 m. If q(k) is less than about 4, the total effective inertia of the rock population will be ≥1700. For example, the 5% model rock distribution has a total effective rock inertia of about 1250 for a q(k) of almost 5.

4.3. Potentially Hazardous Rocks

[33] The effective thermal inertia of rocks versus diameter plot indicates that only rocks with effective inertias of ≥2100 can be considered potentially hazardous as they correspond to rocks with diameters 0.26 m in diameter or greater. This assumes that the rock is a discrete high inertia unit that is hazardous with a height-width ratio roughly >0.5, as flat bedrock (as observed at VL1 [*Moore and Keller*, 1990, 1991]) are not hazardous regardless of their effective thermal inertia. The largest rocks against which the MPF and MER airbags have been tested are 0.5 m high [*Golombek et al.*, 1997a] or those with diameters of ~1 m or greater [*Golombek and Rapp*, 1997]. Note that the size-frequency distributions of rocks measured at the VL1, VL2 and MPF landing sites have <1% area covered by rocks greater than 1 m diameter, even though these sites are among the rockiest on the planet [*Christensen*, 1986a]. For rock populations with a total effective thermal inertia of 1700–2500, as opposed to 1250 assumed by *Christensen* [1986a], less area would be covered by rocks [*Kieffer et al.*, 1973; *Christensen*, 1982, 1986b] for a given bulk inertia. Conversely, any rock observed at VL1, VL2 and MPF whose effective thermal inertia is less than ~2100, should not be considered potentially hazardous.

4.4. Rock Abundance for Different Effective Rock Inertias

[34] To address the change in inferred rock abundance (total area covered by a population of rocks) for different effective rock thermal inertias, a simple thermal model of the bulk inertia of the surface was solved for different rock inertia, rock abundance, and fine component inertia. Rock component thermal inertias of 1300, 1700, 2100, and 2500 were evaluated with a suite of fine component thermal inertias from 77 to 542. This selection of a wide range in rock effective inertia and fine component inertia allows a test of the sensitivity of the derived rock abundance to these derived values (and their uncertainties). As an example, if the maximum effective inertia of a rock >0.26 m in diameter had been assumed in the model to be 2500, then the cumulative effective inertia versus diameter curves would approach 2500 SI units (as opposed to 2100 shown in Figure 15), which is accommodated here by assuming a maximum effective rock inertia of 2500. For each combination of rock and fine component thermal inertias, the surface temperature at 5AM local Mars time for the two materials (rock and fines) was calculated using a standard thermal model [*Mellon et al.*, 2000] and the corresponding black-body spectral emission at these temperatures. For a range of rock abundances (0–50%), we then mixed the corresponding spectral emissions and calculated the resulting 20 μm temperature (using an IRTM equivalent response function). Finally we derived the bulk thermal inertia from the 20 μm temperature using the algorithm of *Mellon et al.* [2000]. (Throughout these calculations we assumed a surface albedo of 0.25, an infrared dust opacity of 0.1, and an atmospheric pressure of 6 mb.) This yields a plot of bulk thermal inertia versus rock abundance for different effective rock inertias along lines of constant fine component thermal inertia (Figure 16).

[35] Figure 16 shows that for changes in effective rock inertia from 1300 to 2500 for any given fine component thermal inertia, the total change in rock abundance for any given bulk inertia is about 20%, which is the uncertainty typically reported for these estimates [*Christensen and Moore*, 1992; *Christensen*, 1986a]. The difference in rock abundance for rocks with effective thermal inertias of 1300 versus 2500 should roughly correspond to the difference in relative area covered by rocks with diameters of 0.15 m versus 0.26 m, respectively. As a check for consistency, the

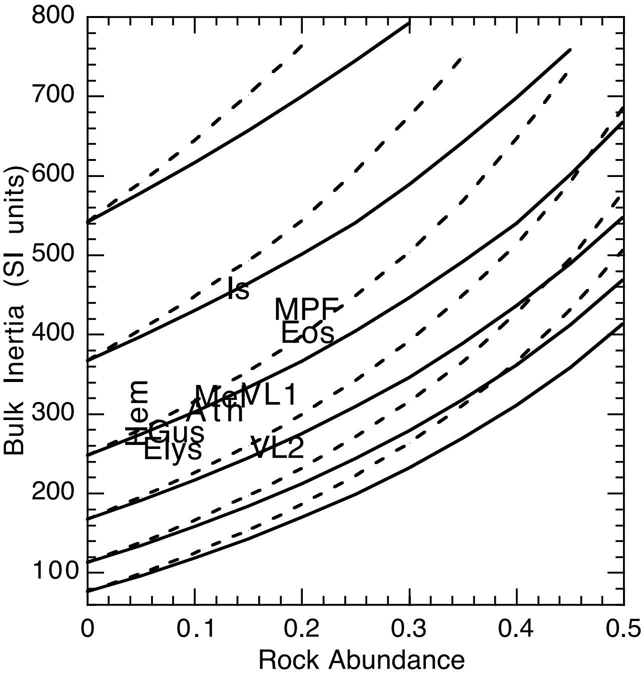

Figure 16. Plot of rock abundance versus bulk thermal inertia for various lines of constant fine component inertia. Solid lines are for effective rock inertias of 1300; dashed lines are for effective rock inertias of 2500. Intermediate values of effective rock inertia (e.g., 1700, and 2100 SI units) fall in between these two for each group of fine component thermal inertia values. Fine component thermal inertia values of 77, 114, 168, 249, 367, and 542 are shown and can be distinguished by where these curves intersect the ordinate or the line of zero rock abundance. Derivation and uncertainties of the plot is described in the text. Landing sites seriously considered for MER (Is is Isidis, Mel is Melas, Ath is Athabasca, Gus is Gusev, Elys is Elysium, and Hem is Meridiani) as well as the Viking and Pathfinder sites are shown for reference using average thermal inertia and rock abundance data shown by *Golombek et al.* [2003].

difference in area covered by rocks of diameter 0.15 m and 0.26 m for the three landing sites is similarly around 25% of the total rock abundance. These results also demonstrate the relative insensitivity of the derived rock abundance to the model of effective rock inertia shown in Figure 14 or to the exact values of the effective rock inertia derived.

[36] The effective inertia of the rock population at the Mars Pathfinder landing site and the areal coverage of the rocks allows the derivation of the expected fine component thermal inertia for the measured bulk inertia. For the bulk IRTM thermal inertia of 435 for the landing site [*Christensen*, 1982, 1986b], the derived effective inertia of the rock population (1700), and the measured areal coverage of rocks (19%), yields a fine component thermal inertia from Figure 16 of 300, which is similar to the IRTM fine component estimate (assuming an effective rock inertia of 1300) of 365 [*Christensen*, 1982, 1986a, 1986b]. This result is also consistent with that derived from the graphical representation of *Kieffer et al.* [1977] used by *Golombek et al.* [1997b, 1999b], modified for the slightly greater rock abundance reported herein.

4.5. Thermal Inertia and Landing Hazards on Mars

[37] Figure 16 also encompasses most of the bulk and fine component thermal inertias for different rock abundances and effective rock inertias possible for mixed soil and rock surfaces on Mars. For reference, the VL1, VL2 and MPF landing sites fall in a zone of 260–440 bulk inertia, 15–20% rock abundance, and resulting fine component thermal inertia of roughly 200 to 340 (with MPF the highest and VL2 the lowest). All of these surfaces are considered safe for the Pathfinder landing system [*Golombek et al.*, 1997a; *Golombek and Rapp*, 1997]. Given our present state of knowledge, we can infer that most areas with <20% rock abundance (among the rockiest 90% of the planet [*Christensen*, 1986a]) and fine component thermal inertia less than about 600 should be acceptable for the Pathfinder landing system [*Golombek et al.*, 1997a]. Figure 16 also shows the landing sites considered for MER [*Golombek et al.*, 2003] and by inference none of these are expected to be unacceptable for the MER landing system.

[38] Figure 16 and the discussion herein also allow us to evaluate the potential hazards of relatively high thermal inertia areas on Mars. Specifically, *Mellon et al.* [2000] and *Jakosky and Mellon* [2001] report surfaces with TES derived bulk thermal inertias that exceed 800 SI units. Some landing sites considered for MER in Valles Marineris have surfaces with bulk inertias this high. These surfaces must have high fine component thermal inertias of 650–800, given that rock abundance does not exceed ~30–35%. Surfaces with fine component thermal inertias this high have generally been interpreted as being duricrust or some other cemented or cohesive surface [*Christensen and Moore*, 1992; *Mellon et al.*, 2000]. Given our previous discussion that argues only materials with effective thermal inertias greater than about 2100 SI units be considered hazardous, none of these surfaces with bulk thermal inertia of up to 800 should be considered especially hazardous a priori, without other information. However, as stated earlier, the hazardousness of surfaces with bulk thermal inertias greater than 800, including the bare rock surfaces discovered by THEMIS [*Christensen et al.*, 2003] cannot be properly evaluated by a simple 2 component model that treats rocks as discrete hazardous objects.

5. Airbag Drop Platform Rock Distributions

[39] To evaluate the capabilities of the MER airbags to successfully cushion the lander during impact, the rock distributions that the airbags were tested against are compared to those likely to be present on Mars. The MER airbags underwent an extensive full-scale airbag drop test program in vacuum, similar to that performed during development of Mars Pathfinder. Around 45 individual drop tests were done at representative impact velocities against a platform with rocks attached (Figure 17). Most tests were done against a 60° dipping platform to simulate grazing impacts likely with significant horizontal velocities, but tests were also performed against platforms dipping 30°, 45°, 72°, and 0° (flat). Between 3 and 10 rocks 0.2 m to 0.5 m high were attached to the platforms. For dipping platforms,

Figure 17. Airbag test platform dipping at 60° in vacuum chamber with rocks attached. Slats that make up platform are ~30 cm wide. Net in background is to constrain bounces of airbag clad lander. Rocks are sharp andesites attached to platform, some with concrete bases. Rocks are covered with chalk to record which rocks produced tears or other failure of the bags.

airbags impacted rocks on the trailing edge of the tetrahedron, estimated to cover an area of 12.5 m^2, and then rolled to impact the face of a tetrahedral airbag (estimated to be one half of the area of the face 8.95 m^2 or 4.48 m^2) for a total impact area of 16.98 m^2. Flat platform drops impacted the face of the airbags or 8.95 m^2. Most of the rocks are sharp volcanic andesites (Figure 17), but concrete rocks made from molds and other simulated rocks were also used. The length, width and height of each rock was measured, parallel and perpendicular to the platform, respectively, to within 1 cm and normalized for the appropriate impact area.

[40] The size-frequency distribution of rocks used in successful MER airbag drop tests is compared to those at the 3 landing sites and the model Mars rock distributions in Figures 18 and 19. The total area covered by all rocks greater than 0.4 m diameter exceeds that at the three landing sites in all cases and in most cases by a factor of 2–6 (Figure 18). Although the distributions of rocks on the test platforms do not match the shape of the landing sites or the 40% model rock distribution, they do represent extreme rock distributions with specific tests exceeding the model and landing site distributions at all diameters, typically by a factor of 2–8 (Figure 19). The number and area of rocks at ~1 m diameter, which is the maximum height (~0.5 m) to which the airbags were designed, exceeds that for all reasonable model distributions. As for the cumulative area distributions, the cumulative number distributions also are extreme compared to VL1, VL2 and MPF landing sites and expected distributions likely on Mars.

6. Shape and Burial Data for Rocks on Mars and Airbag Drop Platforms

[41] MER airbag drop tests have shown that the internal bladder, which maintains the airbag gas under pressure, is susceptible to failure when impacting triangular shaped rocks greater than 0.2 m high. This failure mode appears due to the concentration of stress on the bladder as it deforms over the rock, exceeding the tensile strength of the material in some situations. During Mars Pathfinder airbag tests, the dominant failure mode was due to abrasion and tearing of the bags on sharp rocks (exacerbated by high horizontal velocity at impact). Both airbag designs incorporate 4 abrasion resistant layers over the interior bladder to accommodate tearing, which is more pronounced on sharp, angular rocks and the MER airbags have incorporated a second interior bladder to ameliorate the likelihood of tensile failure on triangular shaped rocks.

[42] The burial of rocks may also affect the success of the airbags. Deeply buried rocks that do not move during impact are more likely to cause both abrasion of the outer layers and tensile stressing of the interior bladder. Perched

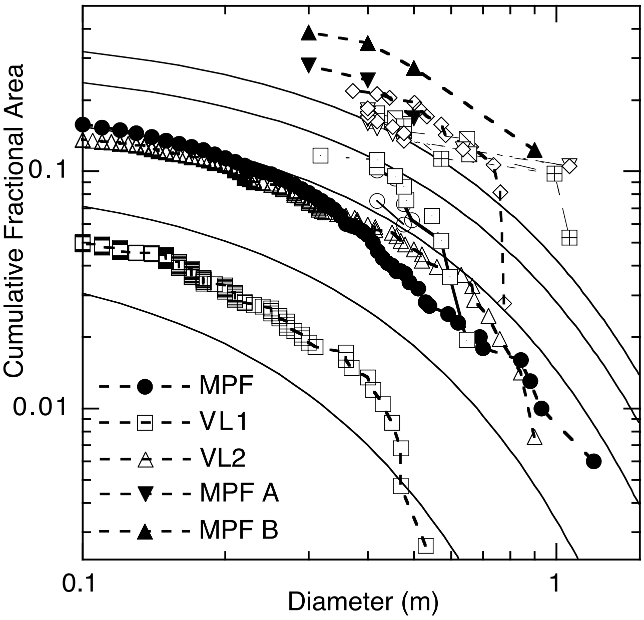

Figure 18. Cumulative fractional area versus diameter of rocks at the VL1, VL2, and MPF landing sites, the size-frequency distribution model, and the airbag drop test platforms used for Mars Pathfinder (MPF A and MPF B) [*Golombek et al.*, 1997a] and a representative sample used for the Mars Exploration Rovers (all others). Rock distributions on the test platforms are extreme. Data for VL1, VL2, and MPF are measured from the near fields. The model rock size-frequency distributions are for 5–40% total rock abundance.

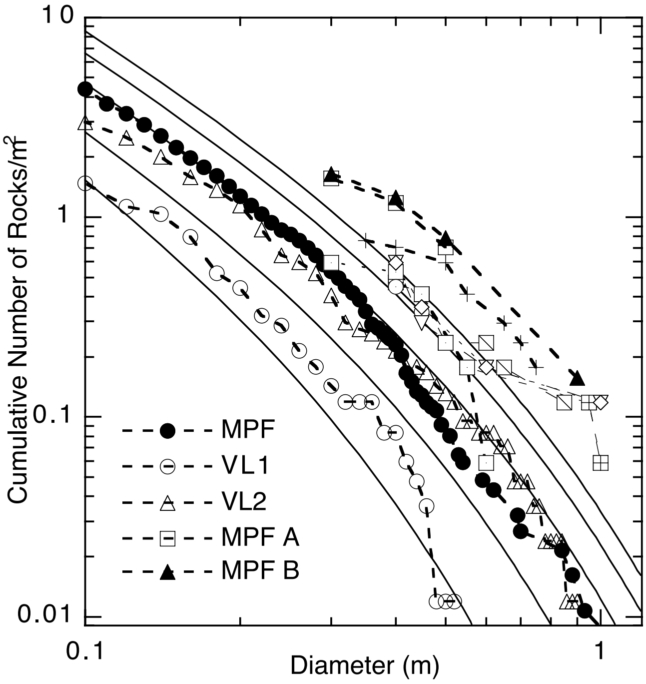

Figure 19. Cumulative number of rocks/m^2 versus diameter at VL1, VL2, and MPF landing sites, the size-frequency distribution model, and the airbag drop test platforms used for Mars Pathfinder (MPF A and MPF B) [*Golombek et al.*, 1997a] and a representative sample of the airbag drop test platforms used for the Mars Exploration Rovers (all others). Rock distributions on the test platforms are extreme. Data for VL1, VL2, and MPF are measured from the near fields. The model rock size-frequency distributions are for 5–40% total rock abundance.

or partially buried rocks that would move during impact would be less likely to tear the exterior airbag layers or stress the interior bladder. To assess these potential failure modes, rocks at the VL1, VL2 and MPF landings sites were characterized according to shape and burial. The shapes of rocks on the airbag test platforms were also characterized (all rocks were firmly attached) to compare with the VL1, VL2 and MPF landing sites on Mars.

[43] Rocks were categorized into 3 shapes shown in Figure 20. Round rocks are similar to hemispheres. Square rocks have large flat horizontal surfaces with distinct edges. Triangular rocks have a distinctly angular or pyramidal shape. Three independent observers evaluated each rock and the rock was classified according to a two-thirds majority. For VL1 and VL2, the comprehensive catalog of rock size and burial within the near and far field (out to 9 m from the landers) prepared by *Moore and Keller* [1990, 1991] and *Baron et al.* [1998] was used. These data sets include the location, length, width, height, and burial of 425 and 499 rocks at VL1 and VL2, respectively, in about 80 m^2 areas. Burial was subjectively determined as perched, partially buried and deeply buried [*Baron et al.*, 1998]. For Mars Pathfinder, the near-field data set described in section 2.2 was used. For VL2, the shape of all rocks with heights greater than 0.2 m were evaluated, which resulted in 28 rocks. For VL1, only one rock is higher than 0.2 m, so the shape of all rocks higher than 0.1 m were evaluated, which resulted in 44 rocks. For MPF, 29 rocks higher than 0.2 m high were evaluated. Data on the shape and burial of rocks at the VL1, VL2 and MPF landing sites can be found in Table 1. Rock

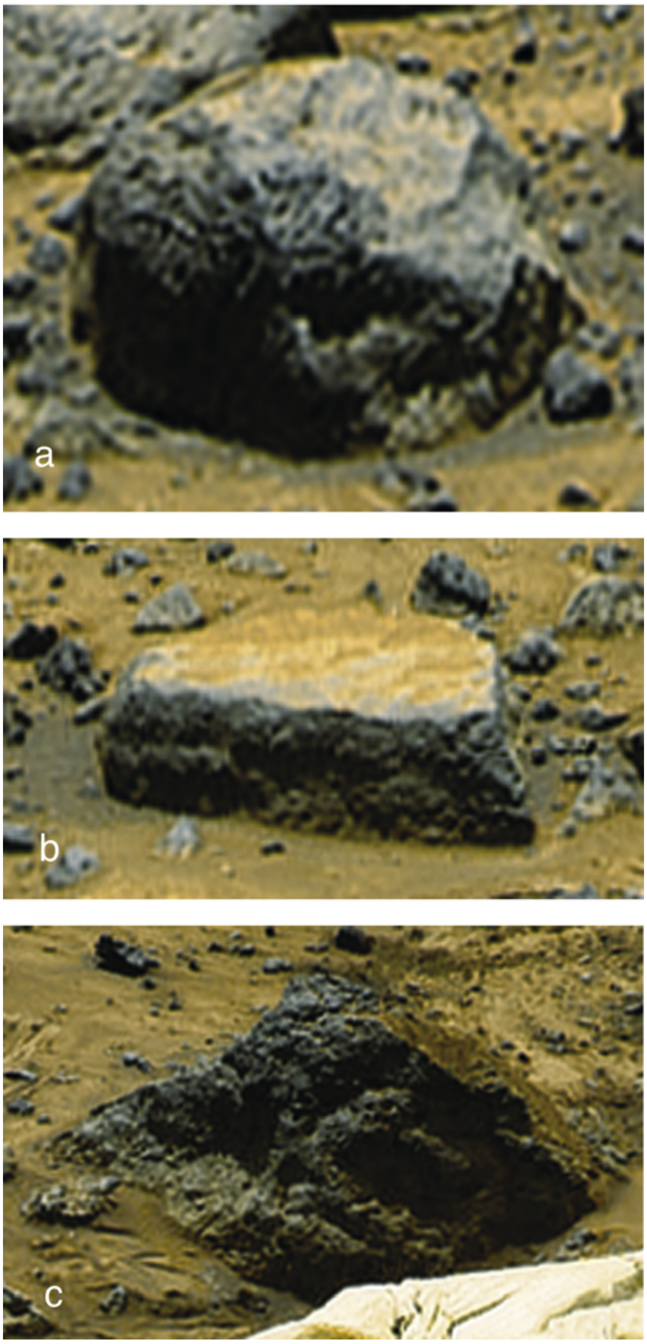

Figure 20. Examples to illustrate the categorization of rock shape at the three landing sites taken from the gallery panorama. (a) Example of a rock (Stimpy, near the Mars Pathfinder lander) categorized as “round”, defined as hemispherical, weathered or smooth. (b) Example of a rock (Flat Top, near the Mars Pathfinder lander) categorized as “square”, defined as having large flat nearly horizontal surfaces with distinct edges. (c) Example of a rock (Minimatterhorn, near the Mars Pathfinder lander) categorized as “triangular”, defined as having a distinctly angular, triangular or pyramid shape.

Table 1. Shape and Burial of Rocks at the VL1, VL2, and MPF Landing Sites[a]

		Number of Rocks								
		Perched			Partially Buried			Buried		
Land Site	H, m	Tri	Sq	Rnd	Tri	Sq	Rnd	Tri	Sq	Rnd
VL1	0.2	1								
	0.1	8	2	6	10	2	10	1	1	3
VL2	0.5						1			
	0.4	1	1	1						
	0.3	1	1	1			2			
	0.2	3		3	1	4	2	3		3
MPF	>0.5		1				1			
	0.4				2					
	0.3		1	1	2	1	1			
	0.2	1	1	4	3	1	6		2	1

[a] VL1 is the Viking Lander 1 site, VL2 is the Viking Lander 2 site, MPF is the Mars Pathfinder Lander site, H is rock height in meters, Tri are triangular shaped rocks, Sq are square shaped rocks, Rnd are round shaped rocks.

shape of all 126 rocks on 16 platforms used to test the MER airbags were also evaluated in a similar manner. These data are shown in Table 2.

[44] Roughly one third of the rocks analyzed at the three landing sites are triangular, similar to the fraction of >0.2 m high rocks that are triangular. Of the rocks >0.2 m high, 15% are buried. This compares with 20%, 29%, and 10% of rocks of all sizes at VL1, VL2 [*Baron et al.*, 1998], and MPF, respectively, being buried. Approximately 19% of all rocks analyzed that are >0.2 m high are triangular and buried or partially buried; 5% of the rocks are triangular and buried. This can be compared to 25% of rocks on the airbag platforms being triangular (and all of these are firmly attached to the platform). To first order, the rocks on the airbag platforms have more triangular and deeply buried (aka firmly attached) rocks than found at the three landing sites. As a result, the airbag drop test rocks represent a greater hazard to the airbags than rocks at the VL1, VL2 and MPF landing sites.

7. Probability of Impacting Potentially Hazardous Rocks

7.1. Introduction and Method

[45] In this section of the paper, we use the model size-frequency distribution of rocks to estimate the probability of impacting a potentially hazardous rock at the landing sites considered for MER. To do this, the rock abundance estimated from thermal differencing techniques [*Christensen*, 1986a] is used to pin the cumulative fractional area covered by rocks >0.1 m in diameter, which is close to k in equation (1). From k, q(k) is calculated from equation (2) and the cumulative fractional area covered by rocks of any given diameter is calculated from equation (1). The cumulative number of rocks/m^2 of any given diameter is derived from the numerical integration of the cumulative fractional area described earlier.

[46] A probability of impact of the airbag-encased lander with rocks of certain sizes and shapes is computed assuming that the number of rocks per unit area at the landing site can be modeled as a Poisson distribution. This application is suggested by the histograms of rocks measured at the VL1, VL2, and MPF landing sites on Mars, which have skewed, long-tailed distributions, and the natural processes that produced these distributions. From the cumulative number of rocks versus diameter model distributions, the number of rocks of a given diameter or greater per unit area, L, is derived. Without other knowledge, L can be assumed to apply across a large area (an IRTM pixel) and can also be assumed to apply to any smaller area, c, regardless of the location of c within the larger area. The probability, p, of a single rock of a given diameter in the area c is approximately proportional to c, when c is small, with the constant of proportionality equal to L. As the subsequent analysis is directed at large, potentially hazardous rocks, the number of rocks of a given diameter is small and thus the probability that two or more rocks in the area c is small in comparison to the probability that one rock is in this area. These criteria formally establish the Poisson distribution as being applicable for the subsequent calculations [*Haight*, 1967]. It should also be noted that for large parameter values (in this case rock diameter), the Poisson distribution approaches the normal (or Gaussian) distribution. Because our application is for a small number of large rocks (beyond the mode of the distribution, which is near 0.05 m diameter), the Poisson distribution is a good approximation for any measured distribution of rocks including lognormal, exponential, or hyperbolic [e.g., *Bagnold and Barndorff-Nielsen*, 1980; *Christiansen and Hartmann*, 1991] and requires the fewest number of assumptions.

[47] It then follows that the probability of exactly n rocks in any area (c L) is expressed as, $P(n, c\,L) = (c\,L)^{\mathbf{n}} \exp(-c\,L)/n!$. The probability that at least one rock of a specified size is within the area c is given by the equation

$$1 - P(0, c\,L) = 1 - \exp(-c\,L). \qquad (3)$$

[48] The calculation assumes that the rock abundance determined from IRTM thermal differencing [*Christensen*, 1986a] is accurate and is made up of individual rocks defined by the model. All rocks are assumed to be hazardous (i.e., they have heights roughly one half of their diameter). No accommodation is made for local variations in the distribution (e.g., clumping) of rocks that might be more hazardous or outcrops (like at VL1) that contribute to the total rock abundance estimate, but are not hazardous. Because of these uncertainties, the calculated probabilities should be considered as best guess statistics.

[49] For each landing site considered, the average rock abundance of pixels that cover a significant portion of the ellipse determined by *Christensen* [1986a], as well as the maximum and minimum (above 2%) are used. Because, the first two bounces are the most energetic, probabilities are calculated for 2, 4, 10 and 60 bounces estimated from

Table 2. Shape of Rocks in Airbag Test Platforms[a]

	Number of Rocks		
H, m	Tri	Sq	Rnd
0.5		4	8
0.4		2	10
0.3	29	51	14
0.2	2	5	1
Total	31	62	33

[a] H is rock height in meters, Tri are triangular shaped rocks, Sq are square shaped rocks, and Rnd are round shaped rocks.

Table 3. Probability of Impacting a Rock >1 m Diameter (8.95–16.98 m^2 Footprint)[a]

Landing Site	IRTM Rock Abundance, %	Cum. Number of Rocks/m^2 >1 m Dia.	Prob, %, 2 Bounces	Prob, %, 4 Bounces	Prob, %, 10 Bounces	Prob, %, 60 Bounces
Meridiani, Elysium (min)	2	0.00001	0.02–0.03	0.04–0.07	0.09–0.17	0.54–1.01
Meridiani, Elysium (ave)	5	0.0004	0.7–1.3	1.4–2.7	3.5–6.6	19.3–33.5
Athabsca (min)	6	0.0005	0.9–1.7	1.8–3.3	4.4–8.1	23.5–39.9
Meridiani (max)	7	0.001	1.8–3.3	3.5–6.6	8.6–15.6	41.5–63.9
Gusev (ave), Gusev, Elysium (max)	8	0.002	3.5–6.6	6.9–12.7	16.4–28.8	65.8–87
Melas, Athabasca (ave)	11	0.003	5.2–9.7	10.2–18.4	23.5–39.9	80–95.3
Isidis (min), Melas (max)	13	0.005	8.6–15.6	16.4–28.8	36.1–57.2	93.2–99.4
VL1, VL2, MPF, Athabasca (max), Isidis (max)	15–16	0.006	10.2–18.4	19.3–33.5	41.5–63.9	96.0–99.8
Eos (min)	17	0.01	16.4–28.8	30.1–49.3	59.1–81.7	99.5–100.0
Eos (max)	22	0.015	23.5–39.9	41.5–63.9	73.9–92.2	99.9–100.0

[a] Prob is probability. Dia is rock diameter. Rock abundance reported for maximum (max), minimum (min), and average (ave) or mean of pixels covering significant areas of the ellipse. VL1, VL2, and MPF rock abundance as measured from the landers; VL1 without the outcrops is 8% rock abundance.

airbag bounce simulations (bounces after the first 10 are unlikely energetic enough to be considered hazardous to the airbags). Each airbag bounce is assumed to cover either 16.98 m^2 or 8.95 m^2, which represent the area the airbags cover when landing with or without significant horizontal velocity.

7.2. Probability of Impacting >1 m Diameter Rock

[50] To start, the probability of impacting a rock >0.5 m high is calculated (Table 3). The airbags were designed to land successfully on rocks up to 0.5 m high. Rocks larger than this are considered potentially hazardous as the stroke of the airbags may be insufficient to keep the lander from bottoming out on the rock. Rocks 0.5 m high are assumed to be about 1 m in diameter. Because all rocks larger than 1 m diameter are considered hazardous, the cumulative number of rocks/m^2 is used in the calculation. The IRTM rock abundance of pixels within the landing site ellipses in the final 4 sites [*Golombek et al.*, 2003] is as follows: TM20B2, Meridiani Average 5% (pixels 1, 6, 6, 7%), EP55A2, Gusev Average 7.5% (pixels 7, 8% plus a small bit of 3%), EP78B2, Elysium Average 5% (7 pixels are 1, 6, 6, 6, 8, 6% plus a small bit of 11%), IP84A2, Isidis Average 14% (pixels 13, 15%). The probability of impacting a rock larger than 1 m diameter at these landing sites as well as VL1, VL2 and MPF is shown in Table 3.

[51] The probability of impacting a >1 m diameter rock for a minimum rock abundance (evaluated at 2% rock coverage, close to the 1% minimum) at Meridiani and Elysium is 0.02–0.03% in 2 bounces, 0.04–0.07% in 4 bounces, and 0.09–0.17% in 10 bounces. The probability of impacting a >1 m diameter rock for the average 5% rock abundance at Meridiani and Elysium is $\sim$1% in 2 bounces, $\sim$2% in 4 bounces, and $\sim$5% in 10 bounces. The probability of impacting a >1 m diameter rock at the maximum for Meridiani (7% rock abundance) is 1.8–3.3% in 2 bounces, 3.5–6.6% in 4 bounces, and 8.6–15.6% in 10 bounces. The probability of impacting a >1 m diameter rock at the average for Gusev and the maximum at Elysium (8% rock abundance) is 3.5–6.6% in 2 bounces, 6.9–12.7% in 4 bounces, and 16.4–28.8% in 10 bounces. These probabilities rise dramatically with increasing total rock abundance, to $\sim$14% in 2 bounces, $\sim$26% in 4 bounces, and $\sim$50% in 10 bounces for 15–16% rock abundance applicable to Isidis.

[52] Because of the rapid decrease in cumulative number/m^2 model rock distribution curves (Figure 11), there are 10 times fewer rocks >1.5 m diameter and 100 times fewer rocks >2 m diameter. As a result the probability of impacting a >1.5 m diameter rock is <0.14% in 2 bounces, <0.27% in 4 bounces, and <0.68% in 10 bounces at Gusev and Elysium (for the maximum rock abundance of 8%). For the Isidis, Viking and Pathfinder sites, these probabilities rise to roughly <2%, <4%, and <10% in the first 2, 4, and 10 bounces, respectively. The probability of impacting a rock >2 m diameter is <0.03%, <0.07% and <0.17% in 2, 4, and 10 bounces, respectively, at maximum rock abundance (8%) areas of Meridiani, Gusev and Elysium. These results suggest that the probability of impacting a >1 m diameter rock during the initial airbag bounces is relatively low at Meridiani, Gusev and Elysium.

[53] MOC images show boulder fields in Gusev crater, Isidis and Elysium that contain more large boulders than indicated by the model distributions (see section 3). The cumulative number of boulders >4 m in diameter in the areas measured varied between 0.00014 and 0.0015/m^2. For the area with the highest concentration of boulders in Gusev, the probability of impacting a rock >4 m diameter is 2.6–5.0%, 5.2–9.7%, 12.6–22.5%, and 55.3–78.3% in 2, 4, 10, and 60 bounces, respectively. For the lower concentration of boulders measured in Gusev, the probability of impacting a rock >4 m diameter is 0.2–0.5%, 0.5–0.9%, 1.2–2.4%, and 7.2–13.3% in 2, 4, 10, and 60 bounces, respectively. Note that rocks larger than this are probably not hazardous as their surface curvature approaches the width of the tetrahedral airbag face for which the airbags react as if impacting a planar surface.

[54] The actual hazardous nature of a rocky surface includes contributions from horizontal winds and wind shear and slopes over the scale of the airbags, which make up the dominant three safety concerns for landing. Calculations of MER landing success using a sophisticated simulation described by *Golombek et al.* [2003] indicate that even a site with relatively low rock abundance can have deleterious interactions with rocks if the horizontal winds and/or shear are high and the slopes steep. These simulations indicate that Meridiani and Elysium, which have very low rock abundance as well as low winds and slopes have slightly more within specification landing events than Gusev and Isidis, which have higher rock abundance and winds. Interestingly, even though Isidis has twice the rock abundance of Gusev they appear to have an equal percentage of out of specification landing events, implying that the landing system (and airbags, specifically) are not very

Table 4. Probability of Impacting a Rock >0.4 m Diameter (8.95–16.98 m^2 Footprint)[a]

Landing Site	IRTM Rock Abundance, %	Cum. Number of Rocks/m^2 >0.4 m Dia.	Prob, %, 2 Bounces All Rocks	Prob, %, 2 Bounces Triangular Rocks	Prob, %, 2 Bounces Triangular/Buried Rocks
Meridiani, Elysium (min)	2	0.007	11.8–21.2	4.1–7.6	0.6–1.2
Meridiani, Elysium (ave)	5	0.03	41.5–63.9	16.4–28.8	2.7–5.0
Gusev, Elysium (max)	8	0.06	91.9–99.2	30.1–49.3	5.2–9.7
VL1, VL2, MPF, Athabasca (max), Isidis (max)	15–17	0.2	99.9–100.0	69.7–89.6	16.4–28.8
Eos (max)	22	0.28	100.0	81.2–95.8	22.2–37.8

[a] Prob is probability. Dia is rock diameter. Rock abundance reported for example maximum (max), minimum (min), and average (ave) or mean of pixels covering significant areas of the ellipse. VL1, VL2, and MPF rock abundance as measured from the landers; VL1 without the outcrops is 8% rock abundance.

sensitive to surfaces with rock abundance between 7% and 14% [*Golombek et al.*, 2003]. Furthermore, even though the boulder fields in the ellipses have a higher density of rocks than the model distributions, which were used in the simulations, they do not add to the out of specification landing events because all the relatively fresh craters (and the ejecta field near the rim) are already assumed to be fatal in the simulations.

[55] The actual probabilities of impacting a rock >1 m diameter certain to be hazardous to the lander is less than the numbers quoted for the following reasons. The airbags have been repeatedly successful in tests against rocks 0.5 m high, and engineering analysis suggests that the likelihood of failure does not increase significantly until the rock height exceeds 0.7 m. Rocks this high, corresponding to 1.5 m diameter rocks, are 10 times less abundant than 1 m diameter rocks and for a rock abundance of 8%, the lander has a less than 1% chance of impacting such a large rock in 10 bounces. For rocks higher than 0.7 m, the hazardous nature of the rock increases slowly with increasing height, as a function of the normal impact velocity, with higher normal velocities producing greater airbag stroke, and orientation of the lander, with tetrahedral corners having less stroke than tetrahedral faces (neither of which can be quantified).

7.3. Probability of Impacting >0.4 m Diameter Triangular Rock

[56] Next the probability of impacting a >0.4 m diameter rock (>0.2 m high) is calculated, which because of the steep rise in the cumulative number/m^2 model rock curves, is significantly greater than for 1 m diameter rocks (Table 4). For an average rock abundance of 5% at Meridiani, Gusev and Elysium, the probability of impacting a >0.4 m diameter rock in 2 bounces is 41–64%. For the maximum rock abundance at these sites, the probability of impacting a >0.4 m diameter rock rises to 92–99%. In contrast, the high rock abundance sites have a 100% chance of impacting a rock of this size in 2 bounces. If the fraction of triangular rocks (considered potentially hazardous) at the low rock abundance (5%) prospective landing sites is similar to that observed at the 3 landing sites (~33%), then there is 16–29% chance of impacting a triangular rock >0.2 m high in the first 2 bounces (Table 4). These numbers rise to 30–49% chance of impacting a triangular rock >0.2 m high in the first 2 bounces for the maximum at Gusev and Elysium. In contrast, the high rock abundance landing sites have a 70–96% chance of impacting a triangular rock during the first 2 bounces. If the percentage of triangular rocks that are buried (considered potentially more hazardous) at the low rock abundance sites is similar to that observed at the 3 landing sites (5%), then the chance of impacting a buried triangular rock >0.2 m high in the first 2 bounces is ~1%, 3–5%, and 5–10% for surfaces covered by 2%, 5% and 8% rocks, respectively. In contrast, the high rock abundance landing sites have a 16–38% chance of impacting a buried triangular rock during the first 2 bounces (Table 4). These results suggest the probability of impacting potentially hazardous triangular rocks that are buried is reasonably low at the Meridiani, Gusev and Elysium landing sites. The actual probabilities of impacting a rock >0.4 m diameter certain to be hazardous to the lander is less than the numbers quoted as bladder failure against triangular rocks occurred in only certain drop tests, likely controlled by where the airbag hit the rock, and this failure mode has been largely ameliorated by the addition of a second airbag bladder.

8. Proximity of Rocks Available for Study During MER Operations

[57] The model rock size-frequency distributions can also be used to calculate the distance over which a rock of sufficient size to analyze with MER instruments will be present or the number of rocks, or probability of encountering a rock of a given size within a particular area. A rock large enough to place the instruments on the Instrument Deployment Device (IDD) up against is probably about 0.1 m in diameter. A rock with enough mass to remain stationary during abrasion by the Rock Abrasion Tool (RAT) has been estimated to be about 0.3 m diameter. The cumulative number of rocks/m^2 larger than 0.1 m and 0.3 m in diameter is taken from the model size frequency distribution for different total rock abundance values at the landing sites and evaluated over 3 different areas (Table 5).

[58] The first area is that in which the instrument deployment device (IDD) can be placed against a rock within the stereo coverage provided by the forward looking hazard cameras (Hazcams). The IDD can reach about 0.7 m in a 90° stereo overlap pie shaped region in front of the rover, estimated to be about 0.38 m^2. This is the area in which a rock measurement can be made early the next sol, without impacting the rest of rover operations for the next sol (a so-called "target of opportunity" [*Squyres et al.*, 2003], or in this case a "sniff and go" sol). The second area is an annulus 0.9 m beyond the obscuration zone of roughly 2.5 m radius created by the rover solar array when imaged from above by the Navcam and Pancam cameras (0.8 m

Table 5. Expected Number or Probability of Rocks >0.1 m or >0.3 m Diameter Within IDD Workspace, Within an Easy Single Sol Rover Drive (~3.5 m), and Within 10 m[a]

Landing Site	IRTM Rock Abundance, %	Cum. Number of Rocks/m^2 >0.1 m Dia.	Probability, %, of at Least One Rock >0.1 m Dia. in IDD Area	Approximate Expected Number of Rocks >0.1 m Dia. in Area Within ~3 Rover Lengths	Cum. Number of Rocks/m^2 >0.3 m Dia.	Expected Number of Rocks >0.3 m Dia. in Area Within ~3 Rover Lengths	Probability, %, of at least One Rock >0.3 m Dia. in Area Within ~3 Rover Lengths	Approximate Expected Number of Rocks >0.3 m Dia. in Area Within 10 m of Rover
Meridiani, Elysium (min)	2	0.9	29.3	16	0.023	0.38	34.8	7
Meridiani, Elysium (ave)	5	1.1	34.5	20	0.084	1.4	79	25
Gusev, Elysium (max)	8	1.8	50.0	33	0.17	2.8	95.7	51
VL1, VL2, MPF, Athabasca (max), Isidis (max)	15–17	3	68.5	55	0.36	6.0	99.9	108
Eos (max)	22	4	78.6	74	0.58	9.7	100	174

[a] VL1, VL2, and MPF rock abundance as measured from the landers; VL1 without the outcrops is 8% rock abundance.

above the rover deck) and is an area that can be reached by an easy rover drive of less than 3 rover lengths (rover wheel base is ~1.4 m). This annulus has an area of ~18.5 m^2 and is used in the calculation of the probability of a target rock for study within a single "approach sol" near the rover in which the rock can confidently be placed within the IDD workspace [*Squyres et al.*, 2003]. The third area is that area within which a rock can be assessed easily within 2 sols, consisting of a "drive" sol, followed by an "approach" sol, in which the rover is positioned so that the rock of interest is within the IDD workspace. This exact area is dependent on the trafficability of the surface, but is easily an area of about 300 m^2, within about 10 m of the rover. This distance is also within a single sol's drive, although placing a rock within the IDD workspace following such a drive would be uncertain. Operationally, after arriving in a new area following a "drive" sol, the rover would take a series of panoramas using the remote sensing instruments (Pancam and MiniTES) [*Squyres et al.*, 2003]. Rocks >0.3 m diameter within 10 m would be easily resolved spatially and spectrally, respectively, by these instruments and could then be accessed by the rover in 2 sols. Although we cannot predict how many rocks will appear interesting enough to warrant further study after a "panorama" sol, we can estimate the number of rocks likely to be present and imaged within an area accessible in 2 sols. The probability of finding a rock within these three areas is calculated using the same method described in the previous section. The expected number of rocks within the larger areas can also be calculated by simply multiplying the cumulative number of rocks/m^2 times the area of interest (Table 5).

[59] Table 5 shows that there is a 29–50% chance of a rock with diameter greater than 0.1 m will be within the IDD work space for even the low rock abundance landing sites (Meridiani, Elysium and Gusev). The high rock abundance landing sites (e.g., Isidis) will have about a 65% chance that a single rock >0.1 m diameter will exist within the IDD work space. These results suggest that on one third to one half of the sols at Meridiani and Gusev, a rock >0.1 m diameter will be present to perform a "sniff and go" sol with minimal impact to that sol's activities. As a result, opportunities for "sniff and go" sols should be frequent at all of the landing sites.

[60] Many rocks >0.1 m in diameter are expected to be within a single easy "approach" sol at all of the landing sites. At the Meridiani landing site, 16–20 rocks of this size will likely be present within about 3 rover lengths. At the Gusev landing site, about 33 rocks >0.1 m diameter should be easily accessible within a single sol's drive. At the high rock abundance sites, more than 55 rocks of this size are expected to be present in this distance.

[61] For rocks large enough (>0.3 m diameter) to remain stationary during abrasion by the RAT, there is a ~80% chance that a single rock will be present within an easy sol rover drive, or "approach" sol at the Meridiani and Elysium landing sites (5% rock abundance). At Gusev there is a 96% chance that a >0.3 m diameter rock will be within an "approach" sol. As a result, for all of the landing sites there is a high probability that a single rock large enough to RAT will be present within about 3 rover lengths. Over larger areas within 10 m of the rover, about 7–50 rocks >0.3 m in diameter are expected to be present at the Meridiani, Elysium and Gusev landing sites. For the higher rock abundance landing sites, such as Isidis, about 100 rocks >0.3 m diameter are expected within about 10 m. These results suggest that rocks large enough to RAT that can be accessed easily within 2 sols and can be distinguished by the Pancam and MiniTES should be abundant at all of the landing sites.

9. Summary

[62] 1) The size-frequency distribution of rocks at the Mars Pathfinder landing site generally resembles that at the Viking 2 landing site, except for rocks <0.2 m diameter, which exceed those at either Viking landing site by a factor of 2–4 (likely due to the different erosional histories of the sites). The total area covered by rocks at the Pathfinder site is 19%, similar to that at both of the Viking sites and that suggested by thermal models, but varies between 7% and 45% in different sectors. The cumulative fractional area covered by rocks versus diameter distribution is similar to that predicted by an exponential model distribution based on the Viking lander rock distributions. The model curves on a log-log plot rise steeply to diameters of 0.5–1 m, where they shallow out to roughly the total area covered by all rocks at about 0.1 m.

[63] 2) Measurement of rare boulder fields in low Sun angle MOC images show similar steep distributions at large diameter, thereby providing further support for the model

rock distributions. The difficulty in recognizing boulders in MOC images of the existing landing sites, which have high rock abundance, is consistent with measurements from the landers and suggests that most of Mars is relatively free of such large rocks.

[64] 3) The effective thermal inertia of natural rock populations is calculated to be between 1700–2100 J m^{-2} $s^{-0.5}$ K^{-1} or SI units using a simple model of effective thermal inertia versus particle size. Only rocks (>0.3 m diameter) with an effective inertia of >2100 should be considered potentially hazardous. Acceptable combinations of bulk inertia and fine component thermal inertia for different rock abundances at the prospective MER landing sites fall within the range of values sampled at the Viking and Pathfinder landing sites and are likely less hazardous with respect to large rocks.

[65] 4) Distributions of rocks mounted to platforms against which full-scale airbag drop tests were successfully conducted are extreme (similar to model distributions with 50–60% rock coverage), compared with the Viking and Mars Pathfinder landing sites and distributions likely to be encountered on Mars. The airbags successfully cushioned the lander against rocks that are 0.5 m high. About 25% of the rocks on the platforms are triangular or pyramidal shaped rocks >0.2 m high, which yielded a higher likelihood of failure due to abrasion of the outer airbag layers and/or tensile failure of the inner bladder.

[66] 5) Roughly one third of the rocks >0.2 m high at the Viking and Mars Pathfinder landing sites are triangular in shape, however, only 19% are triangular and buried or partially buried. Only 5% of the rocks are triangular and deeply buried, compared with 25% of rocks on the test platform. Rocks used in the airbag tests thus represent a greater hazard than rocks at the Viking and Pathfinder landing sites.

[67] 6) The probability of landing on a potentially hazardous rock in 2, 4, 10, or 60 airbag bounces during landing was calculated using the model rock distributions for the appropriate rock abundances at the prospective landing sites. The probability of impacting a >1 m diameter rock is $\sim$1% in 2 bounces, $\sim$2% in 4 bounces, and $\sim$5% in 10 bounces for the average 5% rock abundance at Meridiani and Elysium and roughly 5–6 times higher at Gusev. The probability of impacting >1.5 m diameter rocks, which the airbags are expected to withstand is roughly 10 times lower and <1% in 10 bounces at Meridiani, Elysium and Gusev. The probability of impacting a buried triangular rock >0.2 m high in 2 bounces at Meridiani, Elysium and Gusev is 1–10%, assuming the fraction of buried triangular rocks is similar to the Viking and Pathfinder landing sites. It is likely that only a fraction of these potentially hazardous rocks are actually hazardous, depending on impact velocity and the geometry of the airbags and the rock at impact.

[68] 7) The model rock distributions applied to the prospective landing sites suggest that there is a 30–50% probability that a rock large enough to be measured (>0.1 m diameter) by the spectrometers on the rover should be present within the IDD workspace at the Meridiani and Gusev landing sites. There is about an 80% probability that a rock large enough to be abraded (>0.3 m diameter) can be placed within the IDD workspace in an easy single sol's drive by the rover. On average, more than 50 rocks of this size should be present within 10 m from the rover (easily accessible within 2 sols) at all of the landing sites. As a result, rocks available for study by the rovers should be plentiful at all of the landing sites.

[69] **Acknowledgments.** This work was supported by a grant from the Mars Data Analysis Program from the National Aeronautics and Space Administration at the Jet Propulsion Laboratory, California Institute of Technology. We thank N. Castle, S. Patel, W. Koeppen, L. Evans. N. Breen, W. Clarkson, R. Drummond, D. Jong, and G. Post for measurements of rocks. N. Forsberg-Taylor and R. Schroeder were funded through the SURF program and E. DiMaggio was funded through NASA USRP. We thank R. Craddock and an anonymous reviewer for helpful comments on an earlier version of the paper and S. Squyres for help defining useful operational areas.

References

Anderson, S. W., E. R. Stofan, J. J. Plaut, and D. A. Crown, Block size-distributions on silicic lava flow surfaces: Implications for emplacement conditions, *Geol. Soc. Am. Bull.*, *110*, 1258–1267, 1998.

Bagnold, R. A., and O. Barndorff-Nielsen, The pattern of natural size distributions, *Sedimentology*, *27*, 199–207, 1980.

Baron, J. E., R. A. Simpson, G. L. Tyler, H. J. Moore, and J. K. Harmon, Estimation of Mars radar backscatter from measured surface rock populations, *J. Geophys. Res.*, *103*, 22,695–22,712, 1998.

Barrett, P. J., The shape of rock particles, a critical review, *Sedimentology*, *27*, 291–303, 1980.

Bell, J. F., III, et al., Mineralogic and compositional properties of Martian soil and dust: Results from Mars Pathfinder, *J. Geophys. Res.*, *105*, 1721–1755, 2000.

Bernard, D. E., and M. P. Golombek, Crater and rock hazard modeling for Mars landing, in *Space 2001 Conference, Albuquerque, NM, August 2001* [CD-ROM], *Pap. AIAA-2001-4697*, 17 pp., Am. Inst. Aeron. Astron., New York, 2001.

Brown, W. K., and K. H. Wohletz, Derivation of the Weibull distribution based on physical principles and its connection to the Rosin-Rammler and lognormal distributions, *J. Appl. Phys.*, *78*, 2758–2763, 1995.

Christensen, P. R., Martian dust mantling and surface composition: Interpretation of thermophysical properties, *J. Geophys. Res.*, *87*, 9985–9998, 1982.

Christensen, P. R., The spatial distribution of rocks on Mars, *Icarus*, *68*, 217–238, 1986a.

Christensen, P. R., Regional dust deposits on Mars: Physical properties, age, and history, *J. Geophys. Res.*, *1*, 3533–3545, 1986b.

Christensen, P. R., and H. J. Moore, The Martian surface layer, in *Mars*, edited by H. H. Kieffer et al., pp. 686–727, Univ. of Ariz. Press, Tucson, 1992.

Christensen, P. R., et al., Morphology and composition of the surface of Mars: Mars Odyssey THEMIS results, *Science*, *300*(5628), 2056–2061, 2003.

Christiansen, C., and D. Hartmann, The hyperbolic distribution, in *Principals, Methods and Application of Particle Size Analysis*, edited by J. P. M. Syvitski, pp. 237–248, Cambridge Univ. Press, New York, 1991.

Craddock, R. A., M. Golombek, and A. D. Howard, Analyses of rock size-frequency distributions and morphometry of modified Hawaiian lava flows: Implications for future Martian landing sites (abstract), *Lunar Planet. Sci.* [CD-ROM], *XXXI*, 1649, 2000.

Dobkins, J. E., and R. L. Folk, Shape development on Tahiti-Nui, *J. Sediment. Petrol.*, *40*, 1167–1203, 1970.

Drake, L. D., Rock texture: An important factor for clast shape studies, *J. Sediment. Petrol.*, *40*, 1356–1361, 1970.

Duxbury, E., and D. Jensen, *Vicar User's Guide, Version 3*, *D-4186 Rev B*, NASA, Jet Propul. Lab., Calif. Inst. of Technol., Pasadena, 1994.

Garvin, J. B., P. J. Mouginis-Mark, and J. W. Head, Characterization of rock populations on planetary surfaces: Techniques and a preliminary analysis of Mars and Venus, *Moon Planets*, *24*, 355–387, 1981.

Gilvarry, J. J., Fracture of brittle solids I. Distribution function for fragment size in single fracture (theoretical), *J. Appl. Phys.*, *32*, 391–399, 1961.

Gilvarry, J. J., and B. H. Bergstrom, Fracture of brittle solids II. Distribution function for fragment size in single fracture (experimental), *J. Appl. Phys.*, *32*, 400–410, 1961.

Golombek, M. P., and N. T. Bridges, Erosion rates on Mars and implications for climate change: Constraints from the Pathfinder landing site, *J. Geophys. Res.*, *105*, 1841–1853, 2000.

Golombek, M., and D. Rapp, Size-frequency distributions of rocks on Mars and Earth analog sites: Implications for future landed missions, *J. Geophys. Res.*, *102*, 4117–4129, 1997.

Golombek, M. P., R. A. Cook, H. J. Moore, and T. J. Parker, Selection of the Mars Pathfinder landing site, *J. Geophys. Res.*, *102*, 3967–3988, 1997a.

Golombek, M. P., et al., Overview of the Mars Pathfinder mission and assessment of landing site predictions, *Science*, *278*, 1743–1748, 1997b.

Golombek, M. P., and the Mars Pathfinder Science Team, Overview of the Mars Pathfinder mission: Launch through landing, surface operations, data sets, and science results, *J. Geophys. Res.*, *104*, 8523–8553, 1999a.

Golombek, M. P., H. J. Moore, A. F. C. Haldemann, T. J. Parker, and J. T. Schofield, Assessment of Mars Pathfinder landing site predictions, *J. Geophys. Res.*, *104*, 8585–8594, 1999b.

Golombek, M. P., et al., Selection of the Mars Exploration Rover landing sites, *J. Geophys. Res.*, *108*(E12), 8072, doi:10.1029/2003JE002074, in press, 2003.

Greeley, R., M. Kraft, R. Sullivan, G. Wilson, N. Bridges, K. Herkenhoff, R. O. Kuzmin, M. Malin, and W. Ward, Aeolian features and processes at the Mars Pathfinder landing site, *J. Geophys. Res.*, *104*, 8573–8584, 1999.

Greeley, R., M. D. Kraft, R. O. Kuzmin, and N. T. Bridges, Mars Pathfinder landing site: Evidence for a change in wind regime and climate from lander and orbiter data, *J. Geophys. Res.*, *105*, 1829–1840, 2000.

Haight, F., *Handbook of the Poisson Distribution*, *Publ. Operations Res.*, *11*, 168 pp., John Wiley, Hoboken, N. J., 1967.

Jakosky, B. M., On the thermal properties of Martian fines, *Icarus*, *66*, 117–124, 1986.

Jakosky, B. M., and M. T. Mellon, High-resolution thermal inertia mapping of Mars: Sites of exobiological interest, *J. Geophys. Res.*, *106*, 23,887–23,907, 2001.

Jakosky, B. M., G. W. Finiol, and B. G. Henderson, Directional variations in thermal emission from geologic surfaces, *Geophys. Res. Lett.*, *17*, 985–989, 1990.

Kieffer, H. H., S. C. Chase Jr, E. Miner, G. Munch, and G. Neugebauer, Preliminary report on infrared radiometric measurements from the Mariner 9 spacecraft, *J. Geophys. Res.*, *78*, 4291–4312, 1973.

Kieffer, H. H., T. Z. Martin, A.R. Peterfreund, B. M. Jakosky, E. D. Miner, and F. D. Palluconi, Thermal and albedo mapping of Mars during the Viking Primary Mission, *J. Geophys. Res.*, *82*, 4249–4291, 1977.

Kirk, R. L., et al., Digital photogrammetric analysis of the IMP camera images: Mapping the Mars Pathfinder landing site in three dimensions, *J. Geophys. Res.*, *104*, 8869–8887, 1999.

Krumbein, W. C., Measurement and geologic significance of shape and roundness of sedimentary particles, *J. Sediment. Petrol.*, *11*, 61–72, 1941.

Malin, M. C., Rock populations as indicators of geologic processes (abstract), in *Reports of the Planetary Geology and Geophysics Program—1987*, *NASA Tech. Memo.*, *4041*, 502–504, 1988.

Malin, M. C., Rock populations as indicators of geologic processes (abstract), in *Reports of the Planetary Geology and Geophysics Program—1988*, *NASA Tech. Memo.*, *4130*, 363–365, 1989.

Malin, M. C., and K. S. Edgett, Mars Global Surveyor Mars Orbiter Camera: Interplanetary cruise through primary mission, *J. Geophys. Res.*, *106*, 23,429–23,570, 2001.

Malin, M. C., et al., Early views of the Martian surface from Mars Orbiter Camera of Mars Global Surveyor, *Science*, *279*, 1681–1685, 1998.

Mellon, M. T., B. M. Jakosky, H. H. Kieffer, and P. R. Christensen, High-resolution thermal inertia mapping from the Mars Global Surveyor Thermal Emission Spectrometer, *Icarus*, *148*, 437–455, 2000.

Moore, H. J., and B. M. Jakosky, Viking landing sites, remote-sensing observations, and physical properties of Martian surface materials, *Icarus*, *81*, 164–184, 1989.

Moore, H. J., and J. M. Keller, Surface-material maps of the Viking landing sites on Mars (abstract), in *Reports of the Planetary Geology and Geophysics Program—1990*, *NASA Tech. Memo.*, *4210*, 160–162, 1990.

Moore, H. J., and J. M. Keller, Surface-material maps of the Viking landing sites on Mars (abstract), in *Reports of the Planetary Geology and Geophysics Program—1989*, *NASA Tech. Memo.*, *4300*, 533–535, 1991.

Nowicki, S. A., and P. R. Christensen, Mars surface rock abundance from Thermal Emission Spectrometer (TES) mapping data (expanded abstract), in *The Fifth International Conference on Mars, July 18–23, 1999, Pasadena, CA* [CD-ROM], abstract 6191, Lunar and Planet. Inst, Houston, Tex., 1999.

Parker, T. J., H. J. Moore, J. A. Crisp, and M. P. Golombek, Petrogenetic interpretations of rock textures at the Pathfinder landing site (abstract), *Lunar Planet. Sci.* [CD-ROM], *XXIX*, 1829, 1998.

Pye, K., *Sediment Transport and Depositional Processes*, 397 pp., Blackwell Sci., Malden, Mass., 1994.

Rosin, P., and E. Rammler, The laws governing the fineness of powdered coal, *J. Inst. Fuel*, *7*, 29–36, 1933.

Smith, P. H., et al., Results from the Mars Pathfinder camera, *Science*, *278*, 1758–1765, 1997.

Sneed, E. D., and R. L. Folk, Pebbles in the Lower Colorado River: A study in particle morphogenesis, *J. Geol.*, *66*, 114–150, 1958.

Squyres, S. W., et al., Athena Mars Rover science investigation, *J. Geophys. Res.*, *108*(E12), 8062, doi:10.1029/2003JE002121, in press, 2003.

Stoker, C. R., E. Zbinden, T. T. Blackmon, B. Kanefsky, J. Hagen, P. Henning, C. Neveu, D. Rasmussen, K. Schwehr, and M. Sims, Analyzing Pathfinder data using virtual reality and super-resolved imaging, *J. Geophys. Res.*, *104*, 8889–8906, 1999.

Ward, A. W., L. R. Gaddis, R. L. Kirk, L. A. Soderblom, K. L. Tanaka, M. P. Golombek, T. J. Parker, R. Greeley, and R. O. Kuzmin, General geology and geomorphology of the Mars Pathfinder landing site, *J. Geophys. Res.*, *104*, 8555–8571, 1999.

Widenius, M., and D. Axmark, *MySQL Reference Manual*, O'Reilly, Sebastopol, Calif., 2002.

Wohletz, K. H., M. F. Sheridan, and W. K. Brown, Particle size distributions and the sequential fragmentation/transport theory applied to volcanic ash, *J. Geophys. Res.*, *94*, 15,703–15,721, 1989.

E. N. DiMaggio, Department of Geological Sciences, University of Michigan, Ann Arbor, MI 48109, USA.

N. K. Forsberg-Taylor, Department of Environmental Sciences, University of Virginia, Charlottesville, VA 22904, USA.

M. P. Golombek, A. F. C. Haldemann, and J. R. Matijevic, Jet Propulsion Laboratory, California Institute of Technology, 4800 Oak Grove Drive, Pasadena, CA 91109, USA. (mgolombek@jpl.nasa.gov)

B. M. Jakosky and M. T. Mellon, Laboratory for Atmospheric and Space Physics, University of Colorado, Boulder, CO 80309, USA.

R. D. Schroeder, Department of Geology, California State University, Bakersfield, CA 93311, USA.